PAPER • OPEN ACCESS

Graphene-black phosphorus printed photodetectors

To cite this article: S Akhavan *et al* 2023 *2D Mater*. **10** 035015

View the article online for updates and enhancements.

2D Materials

Graphene-black phosphorus printed photodetectors

S Akhavan[1,4] , A Ruocco[1], G Soavi[1,5], A Taheri Najafabadi[1,6], S Mignuzzi[1], S Doukas[2] , A R Cadore[1],
Y A K Samad[1], L Lombardi[1], K Dimos[1,7] , I Paradisanos[1], J E Muench[1], H F Y Watson[1], S Hodge[1],
L G Occhipinti[1] , E Lidorikis[2], I Goykhman[1,3] and A C Ferrari[1,*]

1 Cambridge Graphene Centre, University of Cambridge, Cambridge CB3 0FA, United Kingdom
2 Department of Materials Science and Engineering, University of Ioannina, Ioannina 45110, Greece
3 Technion—Israel Institute of Technology, Haifa 3200003, Israel
4 Present Address: Institute for Materials Discovery, University College London, Torrington Place, London, WC1E 7JE, United Kingdom.
5 Present address: Institut fur Festkorperphysik, Friedrich Schiller Universitat Jena, 07743 Jena, Germany.
6 Present address: School of Engineering, University of Greenwich, Central Avenue, Chatham Maritime, Kent ME4 4TB, United Kingdom.
7 Present address: Department of Materials Science, University of Patras, 26504 Patras, Greece.
* Author to whom any correspondence should be addressed.

E-mail: acf26@eng.cam.ac.uk

Abstract

Layered materials (LMs) produced by liquid phase exfoliation (LPE) can be used as building blocks for optoelectronic applications. However, when compared with mechanically exfoliated flakes, or films prepared by chemical vapor deposition (CVD), LPE-based printed optoelectronic devices are limited by mobility, defects and trap states. Here, we present a scalable fabrication technique combining CVD with LPE LMs to overcome such limitations. We use black phosphorus inks, inkjet-printed on graphene on Si/SiO$_2$, patterned by inkjet printing based lithography, and source and drain electrodes printed with an Ag ink, to prepare photodetectors (PDs). These have an external responsivity (R_{ext})$\sim$337 A W^{-1} at 488 nm, and operate from visible ($\sim$488 nm) to short-wave infrared ($\sim$2.7 μm, $R_{ext}\sim$48 mA W^{-1}). We also use this approach to fabricate flexible PDs on polyester fabric, one of the most common used in textiles, achieving $R_{ext}\sim$6 mA W^{-1} at 488 nm for an operating voltage of 1 V. Thus, our combination of scalable CVD and LPE techniques via inkjet printing is promising for wearable and flexible applications.

1. Introduction

1.1. Background

Photodetectors (PDs) are key components of video imaging [1], optical communications [2], night vision [3], gas sensing [4] and many other devices.

Their responsivity can be expressed as external [5, 6]:

$$R_{ext} = \frac{|I_{light} - I_{dark}|}{(P_{opt}.A_{PD}/A_{opt})}, \quad (1)$$

or internal [6]:

$$R_{int} = \frac{|I_{light} - I_{dark}|}{(P_{abs}.A_{PD}/A_{opt})}, \quad (2)$$

where I_{light} and I_{dark} are the currents of the PD under illumination and in dark conditions. A_{PD} and A_{opt} are the PD area and the laser spot size. A_{PD}/A_{opt} is a scaling factor that takes into account the fact that only a

fraction of optical power impinges on the PD. P_{opt} is the incident optical power, and $P_{abs} = abs \times P_{opt}$ is the absorbed optical power, where 0< abs <1 is the optical absorption in the PD. Typically, abs <1, since not all incident photons are absorbed ($P_{opt} > P_{abs}$) [6], therefore $R_{int} > R_{ext}$ [6]. R_{ext} describes the overall PD responsivity, including device-related considerations, such as PD design and architecture, light absorption and reabsorption (i.e. the absorption of radiatively recombined photons in the PD photoactive materials), optical reflection from interfaces, optical path in the photoactive area, materials quality, etc [6]. On the other hand, R_{int} provides an estimate of the photodetection efficiency, characterizing the optical-to-electrical conversion process of the absorbed photons [6]. R_{ext} is related to R_{int} as [6]:

$$R_{ext} = R_{int}.abs = \frac{\eta_{int}q\lambda abs(\lambda)}{hc}, \quad (3)$$

where η_{int} is the internal quantum efficiency, i.e. the ratio of the number of charge carriers collected from the photoactive layer to the number of absorbed photons [6], q is the electron charge, λ is the incident light wavelength, h is the Planck constant, and c the speed of light. abs(λ) is wavelength dependent, therefore the spectral response in quantum-type PDs (whereby photons generate electron–hole, e-h, pairs) typically follows the absorption spectrum of the light-absorbing material [6].

The response time (τ_{life}) is the lifetime of the photogenerated charges in the light-absorbing layer [5]. This determines the PD speed, defined as [5, 6]:

$$\tau_{life} = \frac{\Delta n}{QE \times \phi_{in}}, \tag{4}$$

where Δn is the light-induced change in carrier density, QE is the external quantum efficiency, defined as $QE = \eta_{tran} \times \eta_{abs}$ where η_{tran} is the charge transfer efficiency (i.e. the ratio between the flux of charges that contribute to the current and the total light flux that reaches the surface), η_{abs} is the light absorption efficiency (i.e. the percentage of light absorbed by the sample), and ϕ_{in} is the incoming photon flux. The operation wavelength range is the spectral range where the PD is sensitive to incident light [6]. For cameras and video imaging, detection in the visible ($\sim$400–700 nm) with $\tau_{life}\sim$10–50 ms is desired [5]. $R_{ext} >0.1$ A W^{-1} can remove the need of amplifiers (to increase the output with respect to the input signal (i.e. current)) [7], thus decreasing costs [7].

PDs currently in the market are mainly based on Si complementary metal-oxide-semiconductor (CMOS) technology [8]. For applications in the short-wave infrared (SWIR) (1000–2500 nm/1.24–0.5 eV), beyond the Si bandgap (1.1 eV) [6], current technology relies on III-V InGaAs PDs [9]. However, these require complex manufacturing steps (epitaxial growth) [10], cooling to liquid nitrogen [10], and they are rigid [10].

1.2. Layered materials-based photodetectors
Graphene and related materials (GRMs) are promising for PDs [5, 11], and have demonstrated $R_{ext}\sim10^8$ A W^{-1} at 532 nm [12], with response time $\sim10^{-4}$ s [13], 110 GHz speed [14], operation wavelength covering visible to the mid-IR $\sim$3.2 μm [15] and THz [16, 17], and CMOS integrability [18]. Many GRM-based PDs fabricated based on scalable chemical vapor deposition (CVD) approaches [19, 20] were also reported, with $R_{ext}\sim$121 A W^{-1} at 532 nm [20]. $R_{ext} > 10^5$ A W^{-1} was achieved integrating graphene flakes [12] and/or layered materials (LMs), such as MoS$_2$, [21] with PbS [22, 23] and HgTe quantum dots (QDs) [24], with spectral coverage determined by the absorption of the added material (e.g. QDs) [22].

In graphene-based PDs (e.g. metal-graphene-metal PDs [25]), abs(λ) is governed by the wavelength dependent optical conductivity of SLG [26], doping [26], Pauli blocking [26], mobility [27], scattering time [28], device architecture, and substrate, which affects the optical path and the interference of the incident light [25]. In graphene PDs based on photogating (e.g. graphene/QDs [12], graphene/semiconductor [29]), abs(λ) depends on the absorption coefficient profile ($4\pi K/\lambda$) [6] of the light-absorbing material, where K is the imaginary part of the photoactive material [6].

Liquid phase exfoliation (LPE) is a promising route for production of LM-based inks [30–35]. These have been used for printed solar cells [36], sensors [37], transistors [32], supercapacitors [38, 39], and PDs [40]. LPE inks were used to prepare PDs on rigid (e.g. Si) [41] and flexible (e.g. PET(polyethylene terephthalate)) [42] substrates. Challenges in the development of inkjet-printed LPE based PDs stem from the limitations associated with the presence of traps (surface [43, 44] and interface sites [43, 44] formed during LPE), resulting in photocurrent loss [44].

PDs based on solution-synthesized MoS$_2$ on Si/SiO$_2$ were demonstrated [44]. These were prepared by dissolving (NH$_4$)$_2$MoS$_4$ in dimethylformamide:butylamine:aminoethanol (volumetric ratio of 4.5:4.5:1), followed by spin coating on Si/SiO$_2$ and conversion to MoS$_2$ via annealing at 750 $^{\circ}$C and 1000 $^{\circ}$C under Ar/H$_2$ and Ar/S [44]. The MoS$_2$ channel was defined by photolithography (PHL) and dry etching using O$_2$ plasma. The electrodes were fabricated via e-beam evaporation of Au/Ti. However, the PDs in reference [44] showed R_{ext} limited to $\sim$63 μ A W^{-1} at 405 nm [44], due to the presence of defects [44]. These acted as trap states and resulted in a slow (few s) τ_{life}. The current ($\sim10^{-9}$A when the light was turned on) did not recover to the initial level ($\sim3\times10^{-12}$A with light off [44]). τ_{life} improved to $\sim$20 ms by applying a gate pulse $\sim$100 V to discharge the trapped charges [44]. Lateral heterostructures based on LPE MoS$_2$ flakes as photoactive material and $\sim$4 layer graphene (4LG) flakes [40, 45] or Ag paste [46] as electrodes were reported [40, 45, 46], with $R_{ext}\sim$36 μ A W^{-1} and $\tau_{life}\sim$60 ms at 532 nm [46], and 300 mA W^{-1} under white light. Reference [47] reported LPE MoS$_2$ based PDs with $R_{ext}\sim$50 mA W^{-1} at 515 nm and $\tau_{life}\sim$5 ms, using ethyl cellulose to make percolating films with conductivity $\sim1.72\times10^{-2}$ S m^{-1} [47]. Water-based $<$7LG and WS$_2$ inks were used in reference [42] to make vertical heterostructures, resulting in PD arrays. However, these PDs mostly cover visible (405–532 nm) [40, 42, 44–47] with $R_{ext} \leqslant$50 mA W^{-1}, due to photocurrent loss mainly due to traps [43, 44].

Black phosphorus (BP) is a LM interesting for broad-band PDs because of its thickness dependent direct bandgap varying from $\sim$0.3 eV in bulk [48] to $\sim$2 eV in 1LBP [49]. Micro-mechanical cleavage (MC) has been the main approach used to make

BP PDs [50–57]. Reference [56] demonstrated PDs based on BP flakes with thickness ~10 nm [56], working from ~532 to 3390 nm, with R_{ext}~ 82A W^{-1} at 3.39 μm and τ_{life}~0.13 ms. BP was exfoliated on Si/SiO$_2$. A resist layer was patterned via e-beam lithography (EBL) for metallization and evaporation of Cr/Au as contacts [56]. Reference [53] used MC BP (~8 nm thickness), EBL, and electron-beam evaporation to form arrays of metal contacts. Reference [53] demonstrated BP-based PDs for 400–900 nm, with R_{ext}~4.3×10^6 A W^{-1} at 400 nm, ~10^3 A W^{-1} at 900 nm and τ_{life}~5 ms. Reference [50] used a 225 nm thick BP film stacked between two SLGs as top and bottom contacts. To prevent exposure to the environment, this was encapsulated in 18 nm hBN [50]. The PDs had broadband response ~632–3400 nm, with R_{ext}~0.15 A W^{-1} at 632 nm, ~1.43 A W^{-1} at 3400 nm, and τ_{life}~1.68 ns [50]. However, MC usually produces flakes <1 mm [58], without thickness control (random locations of 1L to tens nm flakes) [59, 60], and lacks reproducibility in terms of amount of material, flake size, and number of layers [61–65]. Reference [41] used LPE BP inks to print BP/CVD SLG/Si Schottky junction PDs, with R_{ext}~164 mA W^{-1} at 450 nm, ~1.8 mA W^{-1} at 1550 nm, and τ_{life}~0.55 ms [41]. Si/SiO$_2$ was patterned with EBL, followed by e-beam evaporation of Au and lift-off. The devices were further patterned to make a window to etch SiO$_2$. CVD SLG was then transferred, covering the Au electrode and the Si window [41]. BP was inkjet-printed on the SLG/Si Schottky junction. This process is complex and requires expensive fabrication tools (EBL and e-beam evaporator). Reference [66] reported SLG/LPE BP PDs. Two Au electrodes were evaporated through a shadow mask on Si/SiO$_2$. CVD SLG was wet transferred on the printed LPE BP. The resulting SLG/BP film was transferred on Si/SiO$_2$ with Au electrodes [66]. These PDs had R_{ext}~7.7×10^3 A W^{-1} at 360 nm at 5 V bias, with τ_{life}~7 s and operation wavelength ~360–785 nm [66]. Table 1 compares the results of MC BP and inkjet-printed BP PDs with different device structures [41, 42, 44–47, 50, 52, 53, 56, 67–71, 182–185]. To the best of our knowledge, there are no reports of inkjet-printed PDs with broadband operation from visible (~400–700 nm) to SWIR (~2500 nm), with R_{ext} >1 A W^{-1} in visible and τ_{life}~10–50 m, suitable for video imaging [72].

Printing can be used for large-scale(>1 m^2) [73] fabrication of optoelectronic devices on both rigid [74] and flexible [75] substrates. A variety of printed devices have been reported [76], such as radio-frequency identification tags on paper [77, 78], sensors [79], displays [80], memories [81], and thin-film transistors [32]. Printing was performed with different methods, such as screen [82, 83], gravure [84], flexography [85], and inkjet [32, 86]. Amongst those, inkjet printing is one of the most promising,

because of attractive features such as direct patterning (mask-free) [87, 88] and resolution [89, 90]. The typical printing resolution is ~100 μm for gravure [91], ~100–200 μm for flexo [91], ~100 μm for screen printing [91]. Inkjet printing offers resolution down to ~50 μm [92], which can be made<500 nm by pre-patterning [93]. Inkjet printers can also be used to dispense etching [94] or patterning agents [95].

Here we use inkjet printing to fabricate SLG/BP PDs. CVD SLG is patterned by inkjet printing polyvinylpyrrolidone (PVP) as mask, followed via reactive ion etching (RIE). PVP is rinsed with water. Source-drain Ag electrodes are then inkjet-printed at the end of the SLG channel. LPE BP is inkjet-printed on the channel, followed by encapsulation using Parylene C to prevent BP oxidation [96].

Our PDs have R_{ext} up to ~337 A W^{-1} at 488 nm for 1 V bias, the highest reported to date for inkjet-printed LPE LMs, to the best of our knowledge, see table 1. Our PDs work in the range ~488 nm−2.7 μm, the broadest for inkjet-printed based PDs, to the best of our knowledge, see table 1. Instead of TMDs, which have tuneable indirect band gap in bulk crystals [97] and direct band gap in 1L [98], we use BP, which exhibits thickness dependent direct bandgap from ~0.3 eV in bulk [48] to ~2 eV in 1L [49]. R_{ext} is proportional to the mobility, μ, as [6]:

$$R_{ext} = \frac{\Delta I}{P_{opt}} \frac{\tau_{life} \mu V_{ds}}{L^2}, \qquad (5)$$

with τ_{life} the response time, V_{ds} the bias applied between source and drain, and L the channel length. The term $\frac{\tau_{life} \mu V_{ds}}{L^2}$ is called gain [6]. By increasing μ, the gain increases, which results in higher R_{ext}. Therefore, we use CVD SLG with μ~1700 cm^2 V^{-1}s^{-1}, instead of solution-processed graphene with μ~300 cm^2 V^{-1}s^{-1} as in reference [99].

To demonstrate the viability of our approach for flexible and wearable electronics, we fabricate SLG/BP PDs on polyester fabric, with R_{ext}~6 mA W^{-1} at 1 V and 488 nm, higher than CVD SLG PDs (R_{ext}~ 0.11 mA W^{-1}) on flexible (acrylic) substrates [100], and comparable to CVD MoS$_2$ PDs (R_{ext}~20 mA W^{-1} at 405 nm) with inkjet-printed poly(3,4-ethylenedioxythiophene) polystyrene sulfonate (PEDOT:PSS) on polyethylene naphthalate (PEN) [69], but with surface roughness lower than our fabric. Thus, inkjet lithography is promising for LMs-based optoelectronic devices on textiles.

2. Results

2.1. Inkjet printing

BP bulk crystals are sourced from Smart-elements GmbH. These are then exfoliated as follows. 15 mg are transferred to a mortar and ground for ~20 min to

Table 1. PDs based on MC BP and LPE BP. IP (inkjet printing), EBL , PHL, UVL (UV lithography). t: average LM film thickness.

Fabrication	Properties					
	Spectral range (nm)	R_{ext}(A W^{-1})	Response time (s)	NEP ($WHz^{-1/2}$)	D*(Jones)	References
IP (LPE BP t∼200 nm)	488–2700	337–0.048 (488–2700 nm)	50×10^{-3}	1.68×10^{-10}	10^{11}	this work
IP (LPE MoS$_2$t∼1.9 μm)	white light	0.3	–	–	3.6×10^{10}	[45]
IP (LPE MoS$_2$t∼700 nm)	515	0.05 (515 nm)	5×10^{-3}	–	3.2×10^9	[47]
IP (LPE MoS$_2$t∼1.3 mm)	405–980	63×10^{-6} (520 nm)	20×10^{-3}	–	4.2×10^8	[44]
IP (LPE MoS$_2$t∼50 nm)	532	36×10^{-6} (532 nm)	60×10^{-3}	–	–	[46]
IP (LPE WS$_2$t∼100 nm)	514	0.001(514 nm)	–	–	–	[42]
IP (CVD MoS$_2$t=1L)	405–780	0.02–0.01 (405–780 nm)	1.7	–	4.8×10^7	[69]
IP (LPE WS$_2$ t∼30 nm)/PHL	632	10^{-4} (632 nm)	–	–	–	[70]
IP (LPE BP)/EBL	450–1550	0.164(450 nm)	550×10^{-6}	–	–	[41]
EBL (MC BP t∼8 nm)	640–940	4.8×10^{-3} (640 nm)	4×10^{-3}	–	–	[52]
EBL (MC BP t∼10 nm)	532–3390	82 (3390 nm)	130×10^{-6}	5.6×10^{-12}	–	[56]
EBL (MC BP t∼10 nm)	830	53(830 nm)	–	–	–	[71]
EBL (MC BP t∼30 nm)	400–3750	0.35×10^{-3} (1200 nm)	40×10^{-6}	–	–	[67]
UVL (MC BP t∼60 nm)	635–1550	594–3300 (635–1550 nm)	3×10^{-3}	–	–	[68]
EBL (MC BP t∼8 nm)	400–900	4.3×10^6–10^3 (400–900 nm)	5×10^{-3}	–	–	[53]
EBL (MC BP t∼225 nm)	632–3400	0.15–1.43 (632–3400nm)	1.8×10^{-9}	7×10^{-12}	–	[50]
Abration (WS$_2$t∼30 nm)	625	144×10^{-3} (625 nm)	70×10^{-6}	–	10^8	[181]
Sputtered (WS$_2$t∼4 nm)	450–635	1.68×10^{-3} (450 nm)	–	–	–	[182]
EBL (WS$_2$t∼7.2 nm)	405–635	160×10^{-3} (405 nm)	21×10^{-3}	–	1.4×10^{11}	[183]
MLL (Carbon QDs/MoS$_2$ t=1L)	300–700	377(360 nm)	7.5	–	1.6×10^{13}	[184]
Abration (MoS$_2$t=15– 25 μm)	365–940	1.5×10^{-6} (660 nm)	20–30	–	–	[185]

facilitate subsequent sonication. BP powders are then mixed with 15ml anhydrous isopropyl alcohol (IPA) (Sigma-Aldrich) in a Schlenk flask, sealed with parafilm, and sonicated for 3 h in a 900 W ultrasonic bath (Fisherbrand Elmasonic S 300 Ultrasonic). The BP solution is then centrifuged (H-641 swinging bucket rotor in a Sorvall WX-100) at 4000 rpm (∼6000 g) for 20 min to let the unexfoliated flakes sediment
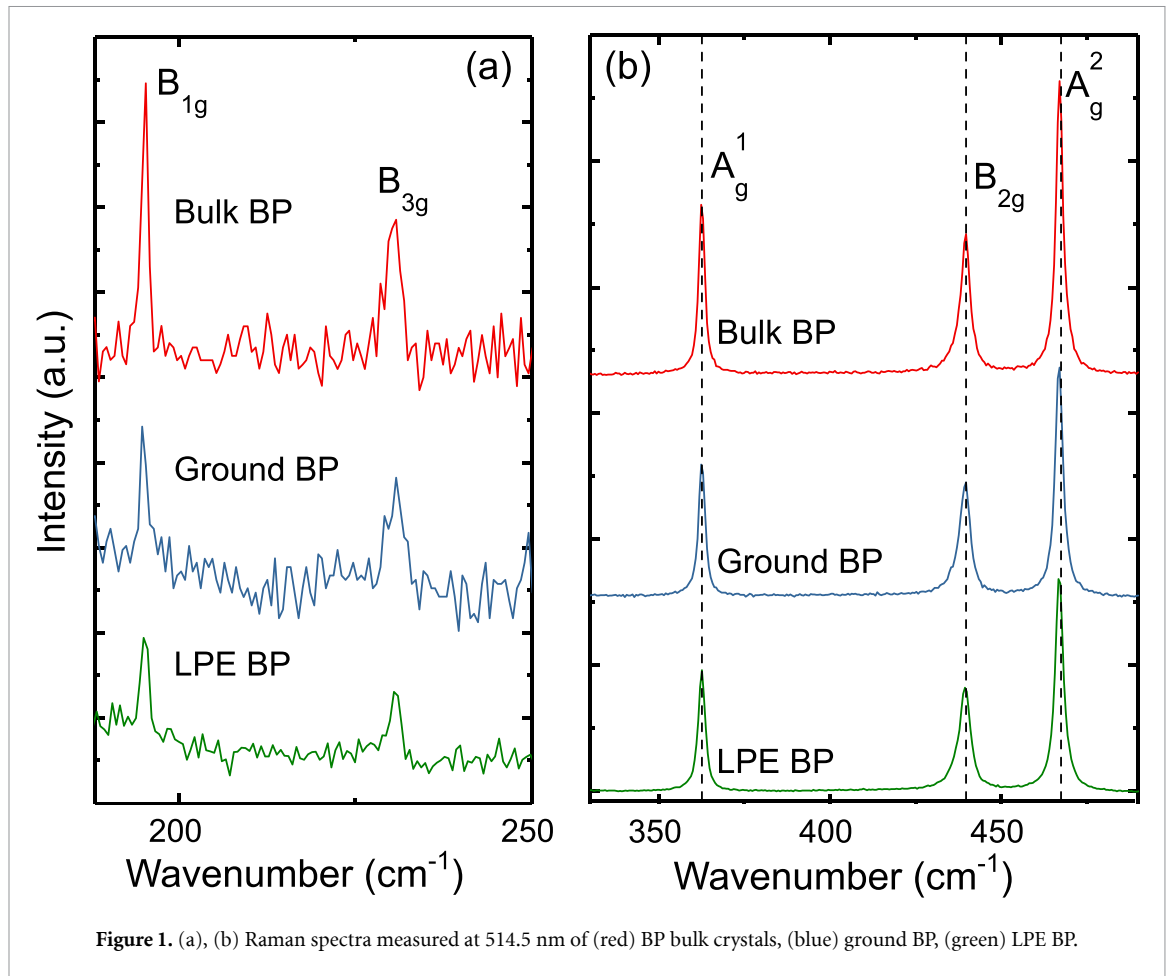
Figure 1. (a), (b) Raman spectra measured at 514.5 nm of (red) BP bulk crystals, (blue) ground BP, (green) LPE BP.

[64, 101]. The supernatant is collected and used for characterization and printing. All procedures are carried out in a glove box (inert atmosphere to minimise BP exposure to the environment or air), except the centrifugation.

The BP crystals are characterized by Raman spectroscopy using a LabRAM HR Evolution equipped with a $100\times$ objective with power on the sample <0.5 mW, to exclude heating effects, figure 1. Bulk BP (red) has three main peaks, figure 1(b). One out-of-plane A_g^1 mode, with position $Pos(A_g^1) \sim 362.6$ cm^{-1} [60, 96, 102–104] and two in-plane B_{2g} and A_g^2 modes, $Pos(B_{2g}) \sim 439.5$ and $Pos(A_g^2) \sim 467.1$ cm^{-1} [60, 96, 102–104]. The corresponding full width at half maximum (FWHM) are $FWHM(A_g^1) \sim 2$ cm^{-1}, $FWHM(B_{2g}) \sim 3.5$ cm^{-1}, $FWHM(A_g^2) \sim 2.5$ cm^{-1}. The peaks ~ 194 and ~ 230 cm^{-1} are assigned to B_{1g} and B_{3g} modes [105]. These are expected to appear when the incident light has a polarization component along the axis orthogonal to the BP layers [106]. However, we detect both, although we are in backscattering, as for previous reports [105–107].

The ground BP sample (blue curve in figure 1) has $Pos(A_g^1) \sim 362.6$ cm^{-1}, $FWHM(A_g^1) \sim 2.1$ cm^{-1}, $Pos(B_{2g}) \sim 439.4$ cm^{-1}, $FWHM(B_{2g}) \sim 3.8$ cm^{-1}, $Pos(A_g^2) \sim 466.9$ cm^{-1} with $FWHM(A_g^2) \sim 2.7$ cm^{-1}, figure 1(b). We observe <0.3 cm^{-1} change in FWHM and $Pos(A_g^1, B_{2g}, A_g^2)$ compared to bulk BP, indicating

the presence of flakes with number of layers, N$>>$6 [96].

The LPE BP flakes (green in figure 1) have $Pos(A_g^1)$ ~ 362.6 cm^{-1}, $FWHM(A_g^1)$ ~ 2.3 cm^{-1}, $Pos(B_{2g})$ ~ 439.3 cm^{-1}, $FWHM(B_{2g})$ ~ 3.9 cm^{-1}, $Pos(A_g^2)$ ~ 466.9 cm^{-1}, $FWHM(A_g^2)$ ~ 2.8 cm^{-1}, figure 1(b). We observe <0.5 cm^{-1} change in FWHM and $Pos(A_g^1, B_{2g}, A_g^2)$ compared to bulk BP, indicating N$>$6 [96].

Stable jetting happens when a single droplet is produced for each electrical impulse, with no secondary droplet formation [92]. This depends on ink viscosity η (mPas) [108], surface tension γ (mNm^{-1}) [108], density ρ (gcm^{-3}) [108] and nozzle diameter D (μm) [109]. A dimensionless figure of merit (FOM) $Z = (\gamma\rho D)^{1/2}/\eta$ was suggested to characterize the stability of inkjetting [108, 109]. [110] reported that if $Z < 1$ the ink would not jet, $Z > 14$ would result in secondary droplets. Therefore, $1 < Z < 14$ is generally considered as the optimal range for stable drop-on-demand [108, 109]. However, we previously showed that drop-on-demand inkjet printing of LM inks with $Z > 14$ is possible [32]. By changing η, γ, and ρ, we are able to tune Z across and outside the conventionally optimal range, and modify our inks for drop-on-demand printing. The size of flakes in solution should be $\sim 1/50 - 1/20$ smaller than the nozzle diameter to prevent clogging [32], and clustering of the particles at nozzle edge [32].

Flakes tend to concentrate at the droplet edge during evaporation, resulting in a ring-like deposit, the so-called coffee-ring effect [111], leading to printing non-uniformity [111]. Adding polymer binders into the LPE dispersion [39, 46, 112] might prevent [39] or alleviate [39] the formation of coffee-rings [39, 46, 112]. However, binders decrease electrical conductivity [39], and must be annealed for removal (e.g. baking on a hot plate at 300 °C–400 °C for ∼1 h [39]). Solvents like N-Methyl-2-pyrrolidone (NMP) are generally the preferred option to disperse BP because of NMP's surface tension and Hansen solubility parameters [31, 113]. However, a temperature close to the NMP boiling point (204 °C) [114]) is required to remove NMP residuals [91], but this can cause oxidation [64, 96] and degradation [64, 96] of air-sensitive BP [41]. NMP is also toxic [115] and can affect the central nervous system [116], so LMs inks dispersed in NMP cannot be used in an open environment [39]. Therefore, it is better to formulate BP inks in nontoxic solvents, with boiling point< 100 °C.

We prepare our BP ink in anhydrous IPA (not as toxic as NMP [121], and commercially available as a 70% solution in rubbing alcohol and hand sanitizers [121]), with a boiling point ∼83 °C [114]. The surface tension and viscosity are characterized via contact angle, surface tension (First Ten Angstroms) and rheometery (Discovery HR-1) measurements at room temperature (RT) and ambient pressure. The BP ink has $\eta \sim 0.55$ mPas, $\gamma \sim 26$ mNm^{-1} and $\rho \sim 0.8$ gcm^{-3}. For printing we use a Fujifilm Dimatix DMP-2800 with D = 22 μm, resulting in Z = 35, outside the conventional optimal range [110]. We aim for BP flake sizes∼1 μm to prevent nozzle clogging [32]. Scanning tunneling electron microscopy (STEM) (Magellan 400 L) is used to measure the flakes lateral size.

Figures 2(a) and (b) are a representative STEM image and a statistical analysis on 140 flakes, indicating mean length ∼220 nm and mean width ∼96 nm. The thickness distribution is estimated by Atomic Force Microscopy (AFM, Bruker Dimension Icon). Figure 3(a) is a typical AFM image of one flake, with thickness ∼5.4 nm, figure 3(b), corresponding to N ∼11. The AFM statistics on 140 flakes shows an average thickness ∼6.7 nm, figure 3(c), corresponding to N ∼13, given a 1 L-BP thickness ∼0.5 nm [122].

Figure 4(a) plots the absorbance, Abs = −log10(Tr) [123], with Tr the transmittance of the BP ink measured with a Cary 7000 UV–VIS–NIR Spectrometer. The BP concentration is estimated from the Beer–Lambert Law [124, 125] $Abs = c \times \epsilon_{ext} \times l$, where c [gL^{-1}] is the concentration, ε_{ext} [Lg^{-1}m^{-1}] the extinction coefficient, and l[m] is the cuvette length [126]. Reference [64] experimentally derived the BP ε_{ext} at 660 nm from the slope of Abs per length
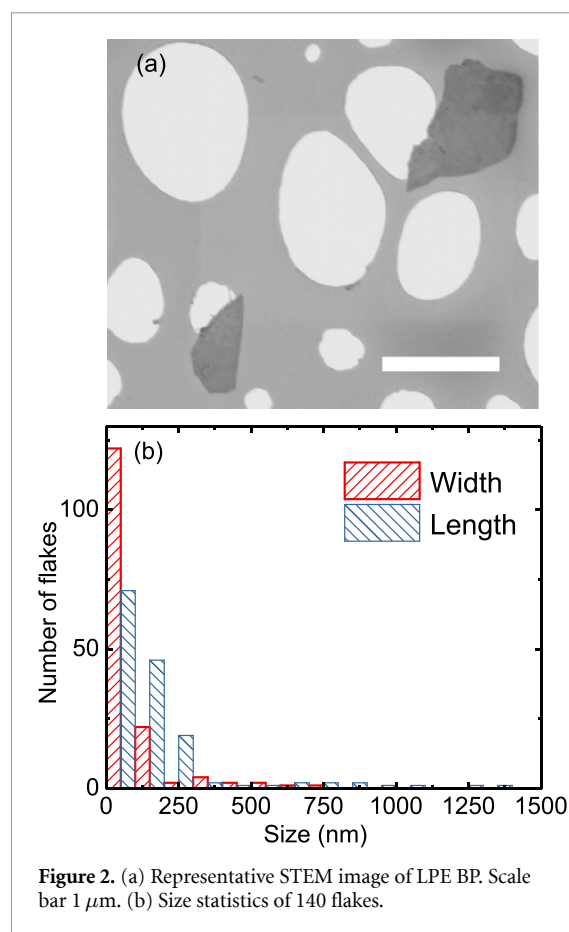

Figure 2. (a) Representative STEM image of LPE BP. Scale bar 1 μm. (b) Size statistics of 140 flakes.

versus the concentration of BP, $\epsilon_{ext} \sim 267$ Lg^{-1}m^{-1}, with c calculated by measuring the weight difference of the collected BP flakes on an anodic aluminum oxide membrane before and after vacuum filtration [64]. From this, we estimate c ∼0.36 gL^{-1} for our ink, similar to reference [64].

High-resolution transmission electron microscopy (HRTEM) images are obtained via a FEI Tecnai F20 FEG TEM operated at 200 keV on BP flakes transferred on holey carbon grids. Figures 4(b) and (c) indicate a crystal plane spacing ∼0.21 nm, corresponding to the (002) plane of orthorhombic phosphorus [117], with N ∼15, and overall thickness ∼7.5 nm, consistent with the flake distribution range obtained by AFM in figure 3(c).

X-ray photoelectron spectroscopy (XPS) (Thermo Fisher ESCALAB 250Xi) is then performed to assess the chemical composition of the BP flakes. The samples for XPS are prepared in an Ar glove box by drop-casting the BP dispersion onto Si/SiO$_2$, followed by N$_2$ gas flushing on a hot plate (60 °C) for ∼5 min. Figure 4(d) shows the $2p^{3/2}$ and $2p^{1/2}$ spin-orbit split doublet ∼129.7 [64, 118] and ∼130.5 eV [64, 118], consistent with previous XPS measurements on bulk BP [119, 127]. The sub-bands ∼134 eV are attributed to surface suboxides introduced during LPE, as for [64, 118].
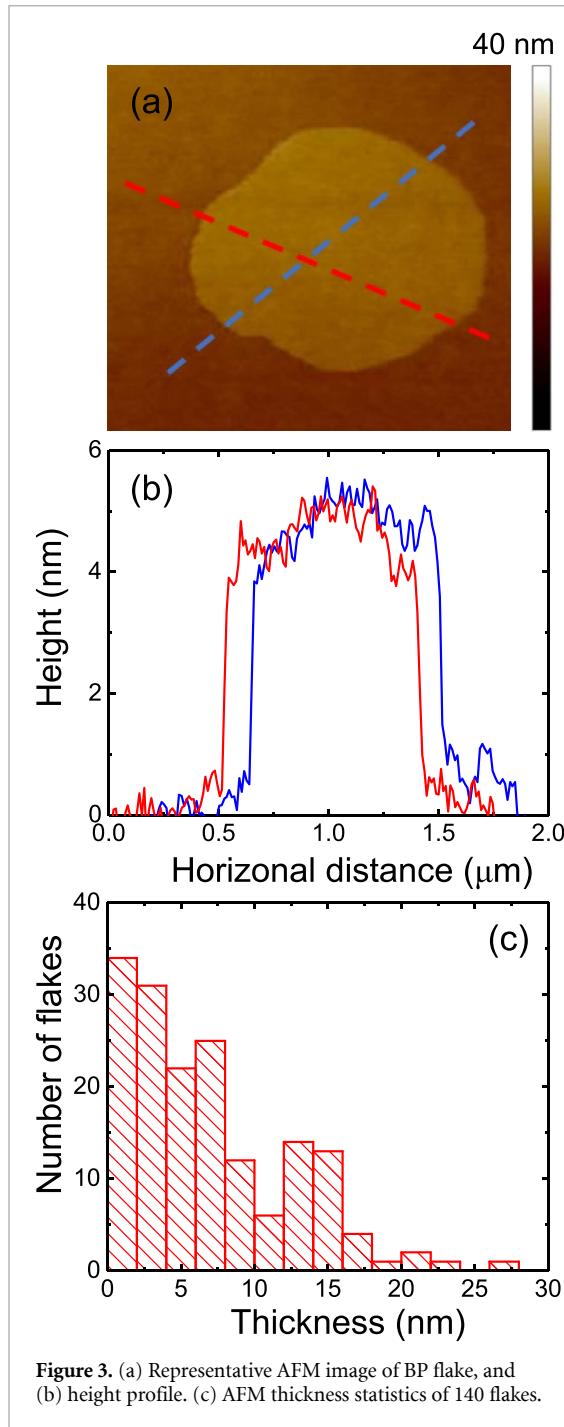
Figure 3. (a) Representative AFM image of BP flake, and (b) height profile. (c) AFM thickness statistics of 140 flakes.

2.2. SLG/BP on Si/SiO$_2$

The design of our SLG/BP PD is shown in figure 5(a). SLG is the channel on Si/SiO$_2$, Si is the bottom gate, SiO$_2$ is the dielectric, BP is the photoactive material, Ag is used for the electrodes, and Parylene C as encapsulation layer. Upon illumination, electron–hole (e-h) pairs are photogenerated in BP. Due to the band alignment (figure 5(b)) h are transferred from the BP valence band (VB) into SLG, leaving behind uncompensated e, acting as an additional negative gate bias, leading to a photogating effect [12]. A schematic band diagram of the SLG/BP interface is in figure 5(b). A built-in field is formed at the SLG/BP interface. Upon BP photoexcitation, h are transferred

to SLG under the built-in field, leaving e trapped in BP. Figure 5(c) is a false color SEM image of the SLG/BP PD.
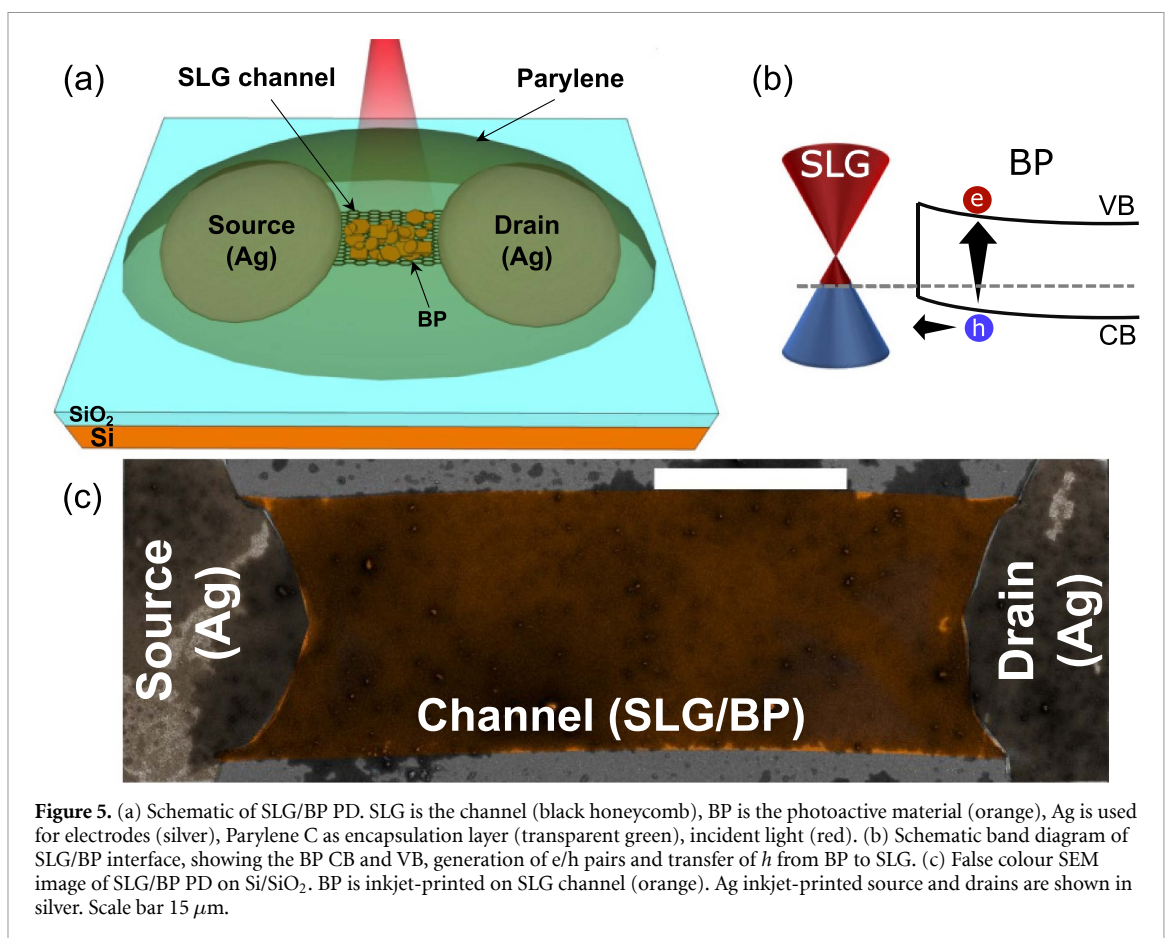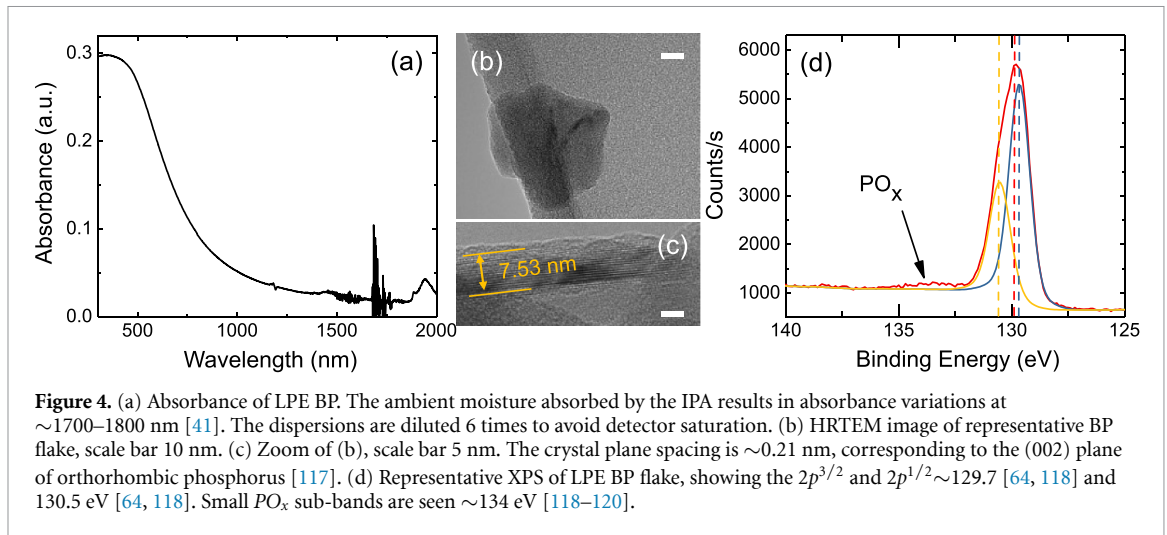
To fabricate the SLG/BP PD, SLG is grown on a 35 μm Cu foil, as for reference [128]. The substrate is annealed at 1000 °C for 30min in the presence of 20sccm H$_2$. To initiate growth, 5sccm CH$_4$ is added. After growth, the sample is cooled to RT at 1mTorr.

The SLG quality is monitored at each step of the fabrication process by Raman spectroscopy. The Raman Spectrum of as grown SLG on Cu is in figure 6, after Cu photoluminescence (PL) removal [129]. The 2D peak is a single Lorentzian with FWHM(2D) $\sim$29 cm^{-1}, signature of SLG [130]. Pos(G) is $\sim$1586 cm^{-1}, with FWHM(G) $\sim$14 cm^{-1}. Pos(2D) is $\sim$2703 cm^{-1}, I(2D)/I(G) and A(2D)/A(G) are $\sim$3.1 and $\sim$6.4. No D peak is observed, indicating negligible defects [131].

The fabrication process flow for SLG/BP PD is outlined in figure 7. To transfer SLG, poly(methyl methacrylate) (PMMA) is spin coated on SLG/Cu, followed by oxygen etching of SLG on the Cu backside, using a RIE-NanoEtch (3 W 30 s). Cu/SLG/PMMA is then left in ammonium persulfate (APS) in DI water for $\sim$6 h until Cu is etched. The resulting SLG/PMMA membrane is placed in DI water to clean the APS residuals and then transferred onto Si+90 nm SiO$_2$, followed by overnight drying and PMMA removal with acetone and IPA, figure 7(a).

The Raman spectrum of SLG transferred on Si/SiO$_2$ is in figure 6. The 2D peak retains its single-Lorentzian line shape with FWHM(2D) $\sim$31.6 cm^{-1}. Pos(G)$\sim$1594 cm^{-1}, FWHM(G)$\sim$11.6 cm^{-1} and Pos(2D)$\sim$2693.1 cm^{-1}, I(2D)/I(G) and A(2D)/A(G) are $\sim$1.2 and 3.2, indicating a p-doping with Fermi energy, E$_F$, $\sim$450 meV [132, 133], which corresponds to a carrier concentration $\sim$12.3$\times$10^{12}cm^{-2} [132]. I(D)/I(G)$\sim$0.06 corresponds to a defect density of $\sim$3.54 $\times$ 10^{10}cm^{-2} [134, 135] for excitation energy 2.41 eV and E$_F$$\sim$450 meV.

Pos(G) and Pos(2D) are also affected by the presence of strain. For uniaxial(biaxial) strain, Pos(G) shifts by ΔPos(G)/Δ $\epsilon_{strain}$$\sim$23(60) cm^{-1}/% [136, 137]. Pos(G) also depends on doping [132, 133]. The average doping as derived from A(2D)/A(G) should correspond to Pos(G)$\sim$1599.2 cm^{-1} for unstrained SLG [132]. However, in our experiments Pos(G)$\sim$1594 cm^{-1}, which implies a contribution from uniaxial (biaxial) strain $\sim$0.22% (0.08%) [136]. Local variations in strain and doping manifest as a spread in Pos(G) and Pos(2D), which in our sample vary from 1592 to 1597 cm^{-1} and from 2688 to 2696 cm^{-1}, figure 8(a). In presence of uniaxial (biaxial) strain, and in the absence of doping, ΔPos(2D)/ΔPos(G)$\sim$2.2 [136, 137]. In our samples ΔPos(2D)/ΔPos(G)$\sim$0.87 (figure 8(a)), which indicates that most of the variation of Pos(G) is due to doping [136, 137]. This is also confirmed by the

Figure 4. (a) Absorbance of LPE BP. The ambient moisture absorbed by the IPA results in absorbance variations at $\sim$1700–1800 nm [41]. The dispersions are diluted 6 times to avoid detector saturation. (b) HRTEM image of representative BP flake, scale bar 10 nm. (c) Zoom of (b), scale bar 5 nm. The crystal plane spacing is $\sim$0.21 nm, corresponding to the (002) plane of orthorhombic phosphorus [117]. (d) Representative XPS of LPE BP flake, showing the $2p^{3/2}$ and $2p^{1/2}\sim$129.7 [64, 118] and 130.5 eV [64, 118]. Small PO_x sub-bands are seen $\sim$134 eV [118–120].

Figure 5. (a) Schematic of SLG/BP PD. SLG is the channel (black honeycomb), BP is the photoactive material (orange), Ag is used for electrodes (silver), Parylene C as encapsulation layer (transparent green), incident light (red). (b) Schematic band diagram of SLG/BP interface, showing the BP CB and VB, generation of e/h pairs and transfer of h from BP to SLG. (c) False colour SEM image of SLG/BP PD on Si/SiO$_2$. BP is inkjet-printed on SLG channel (orange). Ag inkjet-printed source and drains are shown in silver. Scale bar 15 μm.

inverse correlation of FWHM(G) with Pos(G) in figure 8(d) [132, 138, 139].

To pattern the CVD SLG, we use an IPA based PVP ink as mask, to protect SLG during RIE etching. PVP is used due its solubility in IPA [140], stable jetting [92] and ease of removal with water [141]. To make the ink, 5 mg PVP (Sigma-Aldrich) is dispersed in 5 ml IPA. The PVP ink has $\eta\sim$1.25 mPas, as measured with Rheometery (Discovery HR-1), $\gamma\sim$69 mNm^{-1}, as determined with a FTA100 series contact angle and surface tension measurement system (First Ten Angstroms), and $\rho\sim$1 gcm^{-3}, as derived by weighting a known volume of PVP ink via microbalance (Sartorius). For D = 22 μm, Z = 30. We use a Fujifilm Dimatix DMP-2800 to inkjet print PVP, while Si/SiO$_2$ is kept at $\sim$60 °C to promote ink drying. To pattern SLG, PVP is printed on SLG to mask selected SLG regions, figure 7(b). Then, the sample is placed in a RIE to etch the uncovered SLG, figure 7(c). PVP is then removed by adding droplets of water, figure 7(d).
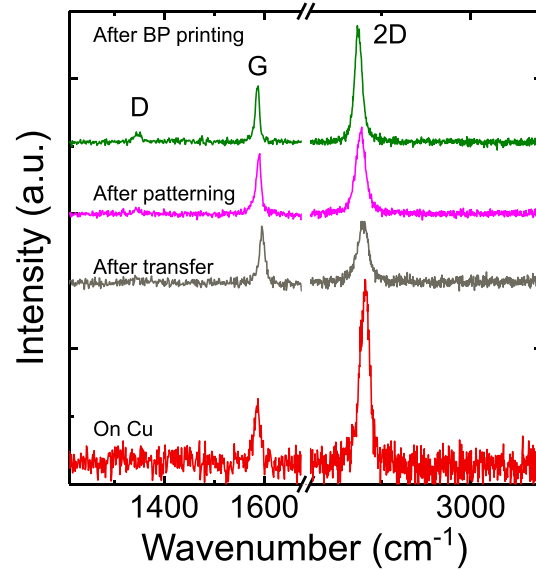
Figure 6. Raman spectra at 514.5 nm of SLG on Cu (red), after transfer (gray), after patterning and PVP removal (purple), and after BP deposition with encapsulation of parylene C and subtraction of the parylene C signal (green). Spectra normalized to have the same I(G).
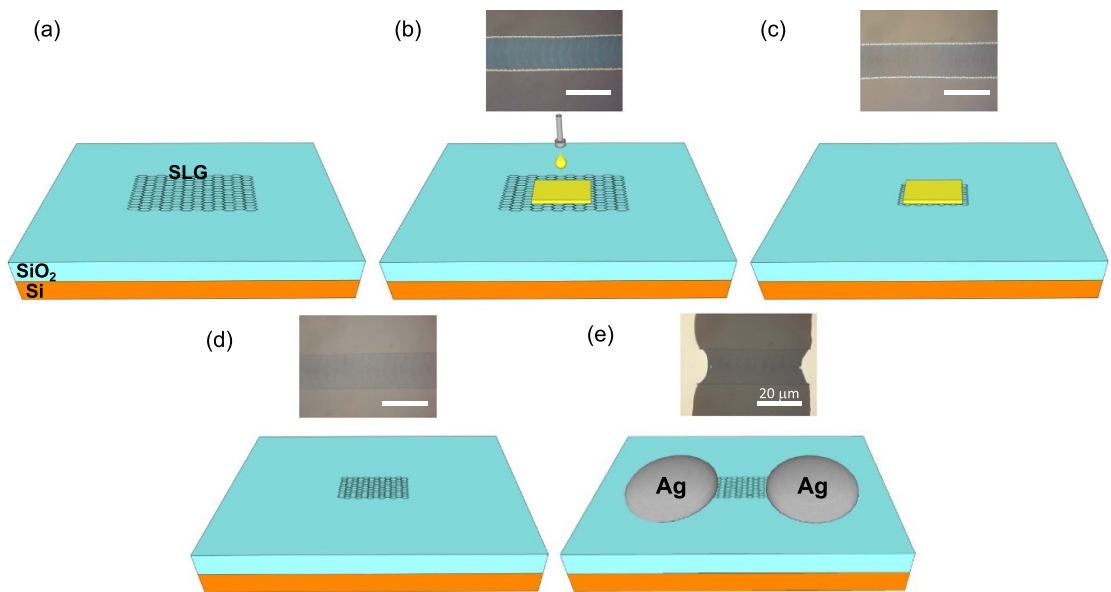

Figure 7. Inkjet lithography of SLG-FET. (a) CVD SLG is transferred on Si/SiO$_2$, followed by overnight drying and PMMA removal using acetone/IPA. (b) PVP (yellow) is inkjet-printed on SLG. The optical microscopy image shows inkjet-printed PVP as mask on SLG. (c) SLG is then etched via RIE. The image shows the PVP ink on SLG after RIE etching. (d) PVP is removed by rinsing with water. The image shows patterned SLG after removal of PVP ink with water. (e) Ag ink (silver) is printed to make source and drain electrodes. The sample is placed on a hot plate at ∼150 °C for ∼2 h. The image shows the inkjet-printed Ag ink after ∼2 h annealing. Scale bars: 20 μm.

The Raman spectrum of etched SLG after PVP removal is in figure 6. The 2D peak retains its single-Lorentzian shape with FWHM(2D) ∼33.7 cm^{-1}. Pos(G)∼1588.1 cm^{-1}, FWHM(G)∼15.6 cm^{-1}, Pos(2D)∼2689.6 cm^{-1}, I(2D)/I(G) and A(2D)/A(G) are ∼1.7 and 3.8, indicating a p-doping with E$_F$∼380 meV [132, 133], corresponding to a carrier concentration ∼8.7×10^{12}cm^{-2} [132]. I(D)/I(G)∼0.08 corresponds to a defect density ∼4.3×10^{10}cm^{-2}

[134, 135] for excitation energy 2.41 eV and E$_F$∼380 meV, thus no significant additional defects are induced during inkjet-lithography. The doping estimated from A(2D)/A(G) should correspond to Pos(G)∼1596.4 cm^{-1} for unstrained graphene [132]. In our experiments Pos(G)∼1588.1 cm^{-1}, which implies a contribution from uniaxial (biaxial) strain ∼0.36% (0.13%) [136]. ΔPos(2D)/ΔPos(G)∼0.34 (figure 8(b)), which indicates that most of ΔPos(G) is
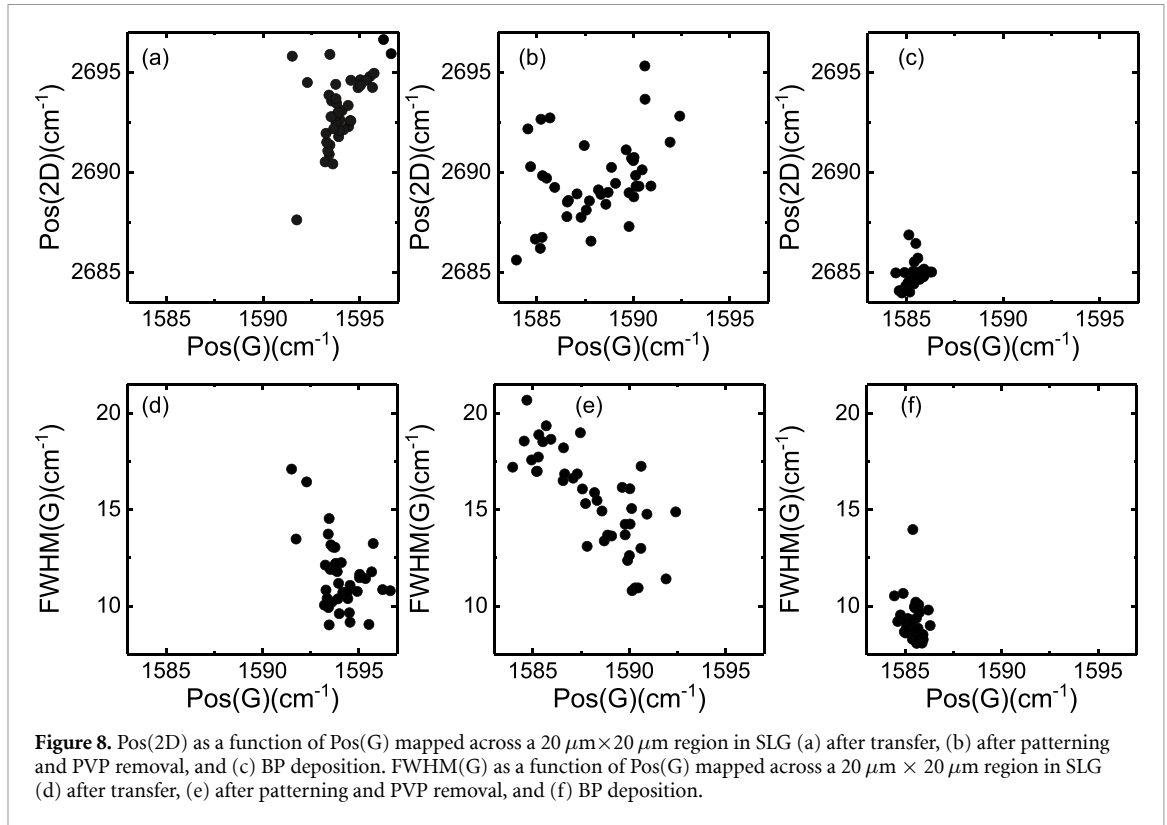
Figure 8. Pos(2D) as a function of Pos(G) mapped across a 20 μm $\times$ 20 μm region in SLG (a) after transfer, (b) after patterning and PVP removal, and (c) BP deposition. FWHM(G) as a function of Pos(G) mapped across a 20 μm $\times$ 20 μm region in SLG (d) after transfer, (e) after patterning and PVP removal, and (f) BP deposition.

due to doping [136, 137], as confirmed by the inverse correlation of FWHM(G) with Pos(G) in figure 8(e) [132, 138, 139].

Source and drain electrodes are then prepared by inkjet printing an Ag ink from Sigma-Aldrich (Ag dispersion, 736465), figure 7(e), with resistivity $\sim$11.2 $\mu\Omega$cm, as measured via a Keithley source meter at the two ends of the channel layer. The linear relation between current and source-drain voltage, V$_{ds}$, indicates an Ohmic contact between Ag and SLG channel, figure 9(a). The resistance of the channel is $\sim$2.07 kΩ. The average sheet resistance, R$_S$, of CVD SLG on Si/SiO$_2$, measured using a 4-point probe method, is R$_S$$\sim$600 $\Omega/\square$. In SLG, R$_S = (\sigma_{2d})^{-1}$ [26], with σ_{2d} the SLG conductivity. In SLG, $\sigma_{2d} = n\mu q$ [142] where n is the carrier density per unit area and q is the e charge. From n$\sim$8.7 $\times$ 10^{12}cm^{-2} derived from our Raman measurements, we get R$_S$$\sim$450 $\Omega/\square$, consistent with our R$_S$ measurements.

We then gate modulate the current between SLG source and drain. SLG shows ambipolar behavior with $\mu$$\sim$1700 cm$^2V^{-1}s^{-1}$, figure 9(b), from [6]:

$$\mu = \frac{\triangle I_d . L}{\triangle V_g . C_{ox} . V_{ds} . W}, \qquad (6)$$

where $\triangle I_d$ is the change in drain current, $\triangle V_g$ is the change in gate voltage, L is the channel length, W is the channel width, and V_{ds} is source-drain voltage. C_{ox} is the gate oxide capacitance $= \epsilon_0\epsilon/t_{ox}$, where $\epsilon_0$$\sim$8.85 $\times$ 10^{-14}F/cm is the vacuum permittivity, $\epsilon$$\sim$3.9 is the dielectric constant of SiO$_2$ [6] and $t_{ox}$$\sim$90 nm is the SiO$_2$ thickness. We use 90 nm SiO$_2$
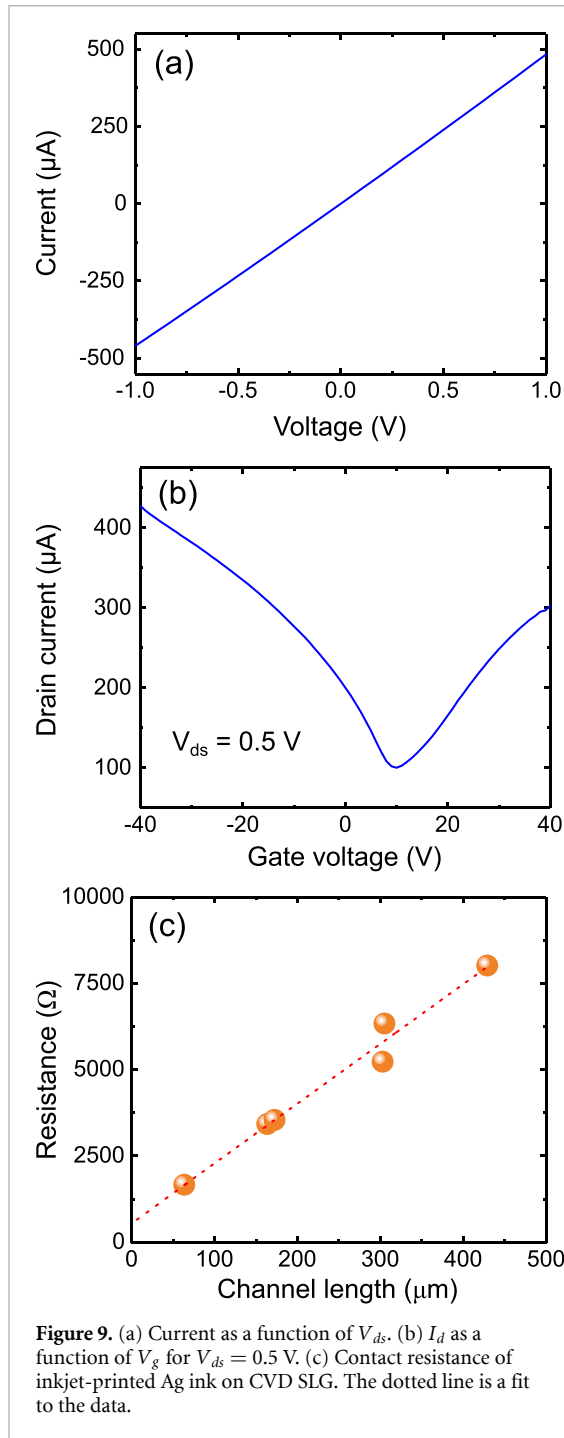
in order to have a larger electric field at lower gate voltages. The SLG quantum capacitance (C_Q) can be calculated as [132, 143]:

$$C_Q \sim \frac{2q^2}{\hbar v_f\sqrt{\pi}}\sqrt{p_{ch}+n_i}, \qquad (7)$$

where $\hbar$ is the reduced Planck constant, $v_f = 1.1 \times$ 10^{6}m/s is the SLG Fermi velocity [59, 144], p_{ch} is the charge carrier concentration per unit area in the channel, and n_i is the intrinsic carrier concentration in SLG near the Dirac point induced by defects and impurities [143, 145–147]. From the Raman analysis we estimate $n_i$$\sim$8.7$\times$10^{12}cm^{-2}. This gives $C_Q$$\sim$6 $\times$ 10^{-6}F/cm^2. Thus, the total capacitance C$_{Tot}$ $= (1/C_{ox}+1/C_Q)^{-1}$$\sim$C$_{ox}$.

The contact resistance (R$_c$) of the Ag printed ink on SLG is estimated from the transfer length method [6], making 6 Ag/SLG/Ag contacts at SLG channel lengths $\sim$60, 160, 175, 300, 305, 430 μm, figure 9(c). R$_c$ of the Ag printed ink on SLG is $\sim$11 KΩ.μm (figure 9(c)). From the linear relation between current and voltage in figure 9(c), we derive an Ohmic contact between Ag and SLG for all 6 samples.

The BP ink is then printed to a thickness $\sim$200 nm to cover the whole SLG channel, as measured with a DektakXT Stylus Profilometer. To prevent BP oxidation and degradation during electrical and photodetection characterizations, the SLG/BP PD is sealed under vacuum using Parylene C dimers (Curtiss-Wright) with a parylene coater (SCS coating). This forms a barrier to moisture and gas permeability [148, 149]. References [41, 96] encapsulated BP flakes

Figure 9. (a) Current as a function of V_{ds}. (b) I_d as a function of V_g for $V_{ds} = 0.5$ V. (c) Contact resistance of inkjet-printed Ag ink on CVD SLG. The dotted line is a fit to the data.

151], CH$_2$ wagging and twisting vibrations [150, 151], CH scissoring in CH$_2$,and/or C-C skeletal in-plane vibrations of the aromatic rings [150, 151], respectively. The 2D peak retains its single-Lorentzian line shape, and narrows from FWHM(2D) $\sim$33.7 cm^{-1} to FWHM(2D)$\sim$23.6 cm^{-1}, figures 6 and 10(c). FWHM(G) narrows from $\sim$15.6 cm^{-1} to $\sim$9.2 cm^{-1}, figures 6 and 10(b). FWHM(2D) and FWHM(G) narrow due to the homogeneous distribution of doping in SLG channel. Pos(G) is $\sim$1585.4 cm^{-1}, Pos(2D)$\sim$2684.8 cm^{-1}, I(2D)/I(G) and A(2D)/A(G) are $\sim$2 and 5.3, indicating a n-doping with E$_F\sim$360meV [132, 133] which corresponds to carrier concentration $\sim$7.7$\times10^{12}$ cm^{-2} [132]. I(D)/I(G)$\sim$0.25 corresponds to a defect density $\sim$13.0$\times10^{10}$ cm^{-2} [134, 135] for excitation energy 2.41 eV and E$_F\sim$360 meV. E$_F$, as calculated from A(2D)/A(G), should correspond to Pos(G)$\sim$1590.2 cm^{-1} for unstrained graphene [132]. We have Pos(G)$\sim$1585.4 cm^{-1}, which implies a contribution from uniaxial (biaxial) strain $\sim$0.21% (0.08%) [136]. ΔPos(2D)/ΔPos(G)$\sim$0.38 (figure 8(c)), which indicates that most of the variation of Pos(G) is due to doping [136, 137]. This is also confirmed by the inverse correlation of FWHM(G) with Pos(G) in figure 8(f) [132, 138, 139].

Since device fabrication comprises many steps, monitoring the quality of graphene is essential, as it could affect μ. The Raman analysis provides information on doping, defects, and strain, which affect μ, thus R_{ext}, as for equation (5). Both compressive and tensile strains can affect μ [152]. [152] reported that a change in strain $\sim$0.012% in CVD SLG resulted in a $\sim$3 times decrease of μ. Our Raman analysis shows a change of strain $\sim$0.01%, from transferred SLG on Si/SiO$_2$, to patterned and BP coated SLG. Thus, we expect μ to decrease $\sim$2 times when going from SLG on Si/SiO$_2$ to patterned and BP coated SLG. This is consistent with field-effect measurements, giving $\mu\sim$1200 cm^2 V^{-1}s^{-1} for SLG on Si/SiO$_2$, reduced to $\sim$650 cm^2 V^{-1}s^{-1} for patterned and BP coated SLG.

Figure 11(a) plots the drain current (I_d) as a function of back gate voltages (V_g),under different optical powers, ranging from $\sim$612 μW to 620 nW. We do not observe light sensitivity$<$620nW, due to no photocurrent generation (photocurrent generation in our SLG/BP PD requires absorption and generation of e-h pairs in BP as photoactive material). Following illumination, V$_D$ shifts to higher V$_g$, and I$_d$ increases for $V_g < V_D$, where carrier transport is h dominated. Therefore, h transfer from BP to SLG is further promoted by gating. Under illumination, light is absorbed by BP and part of the photogenerated h are transferred from the BP VB into lower energy states in SLG, leaving behind uncompensated photogenerated e [68]. The latter are trapped in BP and act as an additional negative gate on the SLG channel, altering the electric field at the SLG/BP junction [68].

with parylene C to prevent BP degradation. Following encapsulation, our SLG/BP PDs are stable for $>$30 days under ambient conditions. Parylene dimers are vaporized at $\sim$80°C. In a separate chamber, they are pyrolysed into monomers at $\sim$690°C. The PD is held at RT, so that parylene polymerizes on contact with the surface, forming a conformal film [41].

The Raman spectra of SLG coated with BP and sealed with Parylene C are in figure 6, and, after subtraction of the parylene C signal, in figures 10(a)–(c). In the Raman spectrum of Parylene C, the peaks $\sim$1207, 1337, 1610 cm^{-1}, figure 10(b), are attributed to CH in-plane vibrations [150,

Figure 10. Raman spectra at 514.5 nm of parylene C (blue) on Si/SiO$_2$ and SLG/BP sealed with parylene C (green) on Si/SiO$_2$.
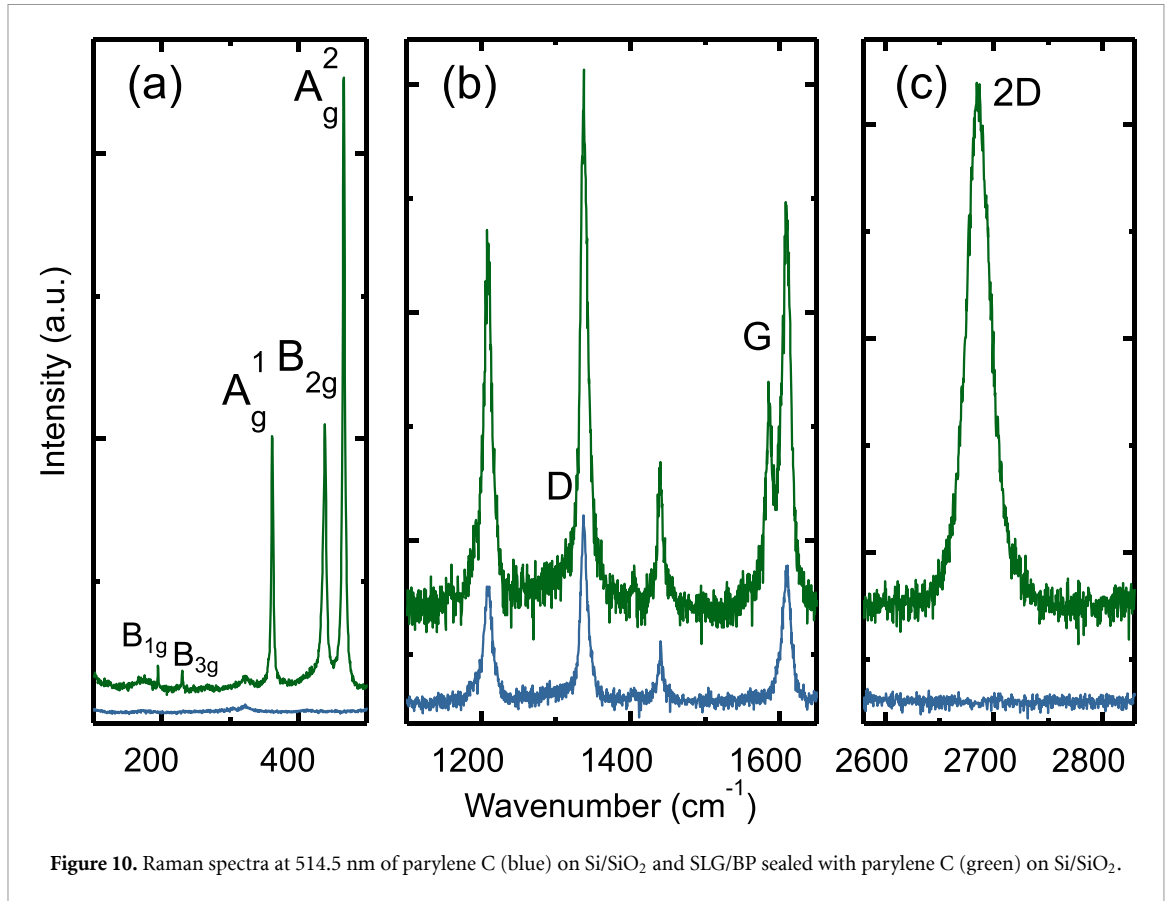
Figure 11(b) plots the photocurrent as a function of V$_{ds}$, defined as [6]:

$$I_{\text{photo}} = I_{\text{light}} - I_{\text{dark}}, \qquad (8)$$

where I_{light} is the current under illumination, and I_{dark} is that in dark conditions. To derive R_{ext}, we measure I_{photo} for powers from ~490 to 1.1 μW, figure 11(c).

Figure 11(c) gives R_{ext}~337 A W^{-1} for 488 nm, when V_g = -20 V ($V_g < V_D$) and V$_{ds}$ = 1 V. For $V_{ds} > 1$ V, the free carriers drift velocity $\nu_d = \frac{\mu E}{1 + \mu E / \nu_{\text{sat}}}$ [153], with ν_{sat} the saturation velocity of the carriers in the SLG channel and E the applied electric field to SLG, increases linearly, until saturation, due to carrier scattering with optical phonons [154]. Therefore, all measurements are done at $V_{ds} \leqslant 1V$ to keep the device operation in the linear (Ohmic) regime, thus eliminating the nonlinear dependence of ν_d on V_{ds}. Figure 11(c) shows that R_{ext} saturates for incident optical power$<1\,\mu$W. For P$_{\text{opt}}$~1.1 μW the number of photogenerated carriers decreases, resulting in an increases of the built-in field at the SLG/BP interface [12, 68], which explains the enhancement of R_{ext} at lower optical powers [12, 68].

Figure 12 plots the spectral R$_{\text{ext}}$ for SLG/BP PDs. These show broadband R$_{ext}$ from visible (488 nm, ~ 300A W^{-1}) to mid-infrared (2700 nm, ~48 mA W^{-1}) at 1 V.

Metal-SLG-metal PDs were reported with R_{ext} of few mA W^{-1} at 633 nm [155] and 1550 nm [156].

The difference in R_{ext} between these and our SLG/BP PDs is attributed to the contribution of the BP photoactive layer. To get a better understanding of spectral response versus wavelength, we perform optical simulations. We extract the BP refractive index from the solution absorbance of LPE BP, figure 4(a). Specifically, transmission in solution can be defined either by the absorbance (Abs = $c \times \epsilon_{\text{ext}} \times l$ as T$_r$ = $10^{-c\epsilon_{\text{ext}}l}$) or by the optical depth as e^{-al} [157, 158], where l is the cuvette length and a = a$_{BP}$c/ρ, a$_{BP}$ = $4\pi K_{BP}/\lambda$ is the BP bulk absorption coefficient, K_{BP} is the imaginary part of the BP refractive index, ρ is the BP density (2340 gL^{-1} [159]), and λ is the incident wavelength. We assume BP flakes randomly oriented, thus seek to extract the average refractive index [160]. Then, K_{BP} = $\epsilon_{ext}\lambda\rho/4\pi\log_{10}(e)$ and the real part of the average refractive index is found by applying the Kramers–Kronig (KK) relation [160], $n_{BP}(w)$ = 1 + 2π^{-1} $\mathcal{P} \int_0^\infty w' K_{BP}(w')/(w'^2 - w^2)\,dw'$, where $\mathcal{P}$ denotes the principal value of the integral and w is angular frequency. The absorbance data of figure 4(a) are truncated at UV = 300 nm, due to the cuvette absorbance ~300 nm [161], making our n_{BP} extraction qualitative, because of the finite integration range. We use the extracted BP refractive index in Fresnel equation calculations [162] to estimate the absorption of SLG/BP on Si/SiO$_2$. The SLG refractive index is modelled by the Kubo conductance [163] at RT and E$_F$ = 0.38 eV, as estimated by the Raman measurements in figure 6. Due to the fluctuations in
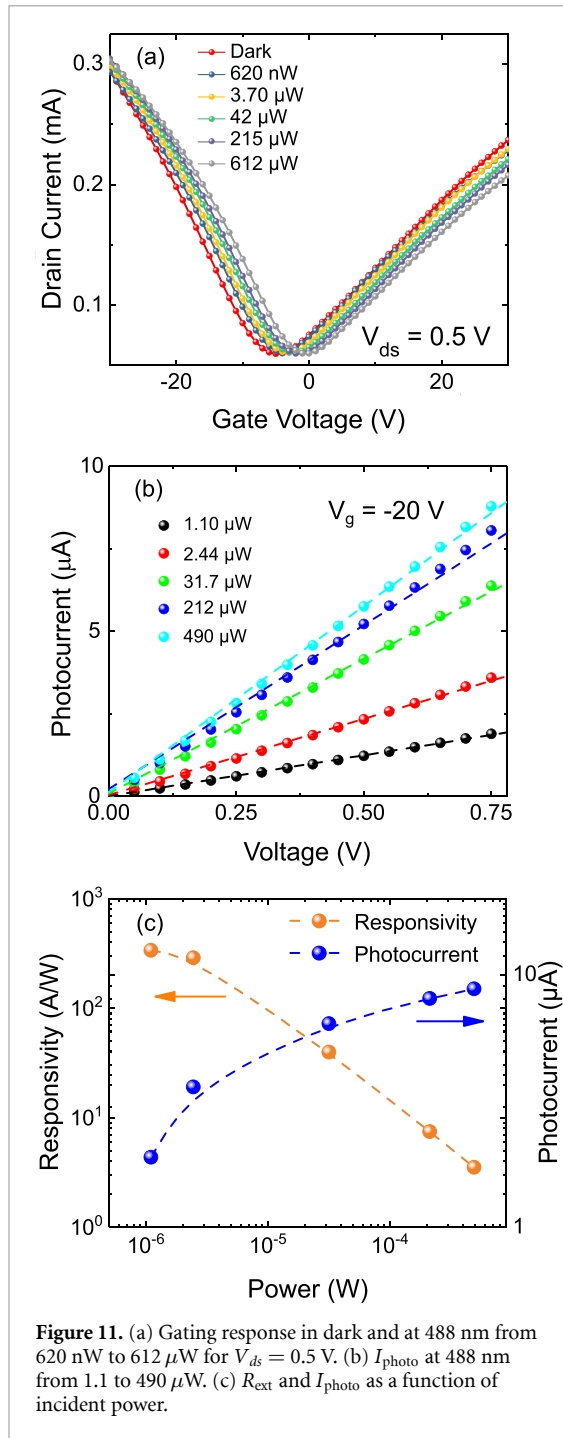
Figure 11. (a) Gating response in dark and at 488 nm from 620 nW to 612 μW for $V_{ds} = 0.5$ V. (b) I_{photo} at 488 nm from 1.1 to 490 μW. (c) R_{ext} and I_{photo} as a function of incident power.
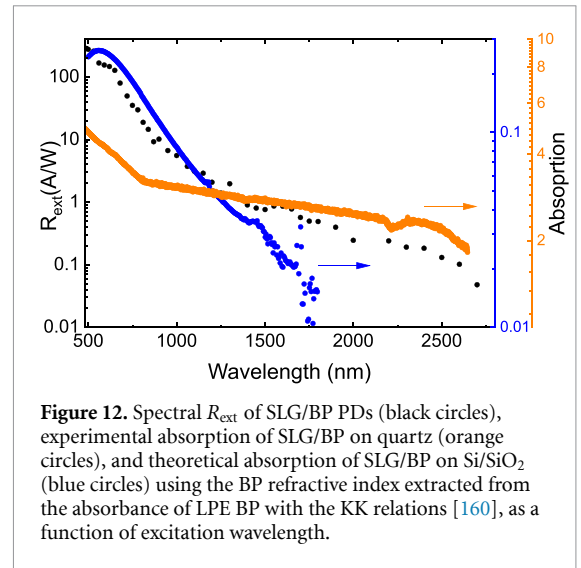

Figure 12. Spectral R_{ext} of SLG/BP PDs (black circles), experimental absorption of SLG/BP on quartz (orange circles), and theoretical absorption of SLG/BP on Si/SiO$_2$ (blue circles) using the BP refractive index extracted from the absorbance of LPE BP with the KK relations [160], as a function of excitation wavelength.
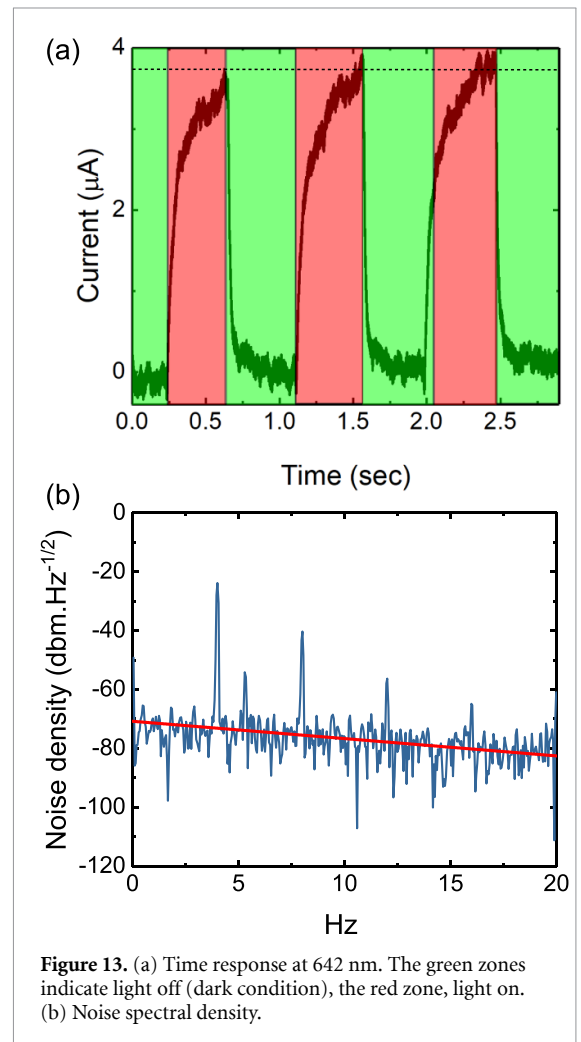

Figure 13. (a) Time response at 642 nm. The green zones indicate light off (dark condition), the red zone, light on. (b) Noise spectral density.

absorbance beyond 1700 nm, figure 4(a), we do not extract refractive index for BP beyond 1700 nm. The experimental absorption of inkjet-printed BP/SLG on quartz is plotted in figure 12. This follows the experimental and theoretical absorption spectra of SLG/BP films, i.e. drop of both R$_{ext}$ and absorption with increasing wavelength, indicating R_{ext} follows the absorption spectra of the light-absorbing photo-active material.

The temporal response of our PDs is then measured with a MSO9404A Mixed Signal Oscilloscope, figure 13(a). The time response in figure 13(a) reaches saturation at $\sim$3.8 μA, as shown by the horizontal dashed line. We thus fit the temporal response decay

in figure 13(a) with [72]: I(t) = A$_0$.exp(-t/τ_{life}) + B, where A$_0$ is the initial current, τ_{life} is the response time and B a constant. We get a response time $\sim$50 ms, two orders of magnitudes faster than the LPE BP/CVD SLG PD of reference [66], consistent with other LPE based PDs [44, 164], but two orders of magnitude slower than the Schottky junction PDs of reference

[41], with lower $R_{ext} \sim 164$ mA W^{-1} at 450 nm, due to lack of photoconductive gain, but faster response time $\sim 550\,\mu s$, because of the Schottky diode characteristics at the Si/SLG/BP interfaces [41].

By applying V$_{ds}$, transferred photogenerated h drift to the drain with a timescale τ_{transit} [6]:

$$\tau_{\text{transit}} = \frac{L^2}{\mu V_{ds}}, \tag{9}$$

where $L = 60\,\mu m$ is the length of channel, and $\mu \sim 1700$ cm^{2}V^{-1}s^{-1}. We thus get $\tau_{\text{transit}} \sim 37$ ns, resulting in a photoconductive gain [6]:

$$\text{Gain} = \frac{\tau_{\text{life}}}{\tau_{\text{transit}}} \sim 10^6. \tag{10}$$

The dependence of R_{ext} on $\frac{\tau_{\text{life}}}{\tau_{\text{transit}}}$ explains the decrease in R$_{ext}$ when the optical power increases. The decrease in R$_{ext}$ suggests an increase of $\tau_{transit}$ and/or decrease of τ_{life}. The increase of τ_{transit} is likely due to increase in scattering of photogenerated carriers in the channel with increase in optical power [165]. Auger recombination induced by increasing power can also increase the photogenerated charges recombination rate, reducing τ_{life} [165]. The gain can be further defined as the ratio of photogenerated currents recirculating in the SLG channel to the injected h from BP to SLG [68]:

$$\text{Gain} = \frac{|I_{\text{light}} - I_{\text{dark}}|}{q.A_{\text{PD}}.\triangle p_{ch}}, \tag{11}$$

where $\triangle p_{ch}$ is the concentration per unit area and per unit time of the injected h. $\triangle p_{ch}$ is equal to the trapped e concentration per unit area and per unit time in BP, related to a charge neutrality point shift $\triangle V_g = \triangle V_D$ in the transfer characteristics (I$_d$ versus V$_g$). To calculate $\triangle p_{ch}$, we consider the potential balance in the metal-dielectric-SLG structure. V_g creates a potential drop ($V_{ch} = E_f/q$) so that [6, 132]:

$$V_g = V_{ch} + V_{\text{diel}} = \frac{E_f}{q} + \frac{Q_G}{C_{ox}}, \tag{12}$$

where Q_G is the charge concentration. $|Q_G| = |q.p_{ch}|$, with p_{ch} the charge carrier concentration per unit area in the channel induced by V_g. Any variation in p_{ch} changes Q_g and V_g. The derivative of V_g with respect to Q_g gives:

$$\frac{dV_g}{dQ_g} = \frac{1}{C_{ox}} + \frac{dV_{ch}}{dQ_g} \tag{13}$$

which results in:

$$\triangle Q_g = \left(\frac{1}{C_{ox}} + \frac{1}{C_Q} \right)^{-1}.\triangle V_g. \tag{14}$$

To find Q_G and $\triangle p_{ch}$, C_{ox} and C_Q are needed. $C_{ox} \sim 38.35 \times 10^{-9} F/cm^2$. From equation (7), we get $C_Q \sim 6 \times 10^{-6} F/cm^2$. Therefore, $\triangle p_{ch}$ varies from $\sim 2.6 \times 10^{11} cm^{-2}$ to $1.1 \times 10^{12} cm^{-2}$ for optical power 620nW to 612 μW at $V_{ds} = 0.5V$. Then, from equation (11), we get Gain $\sim 2 \times 10^6$, in agreement with equation (10).

We then evaluate the detectivity (D^*) [$cm.Hz^{1/2}/W$ or Jones]. This relates the performance of PDs in terms of R$_{ext}$ to A$_{PD}$, allowing the comparison of PDs with different A$_{PD}$ [6]:

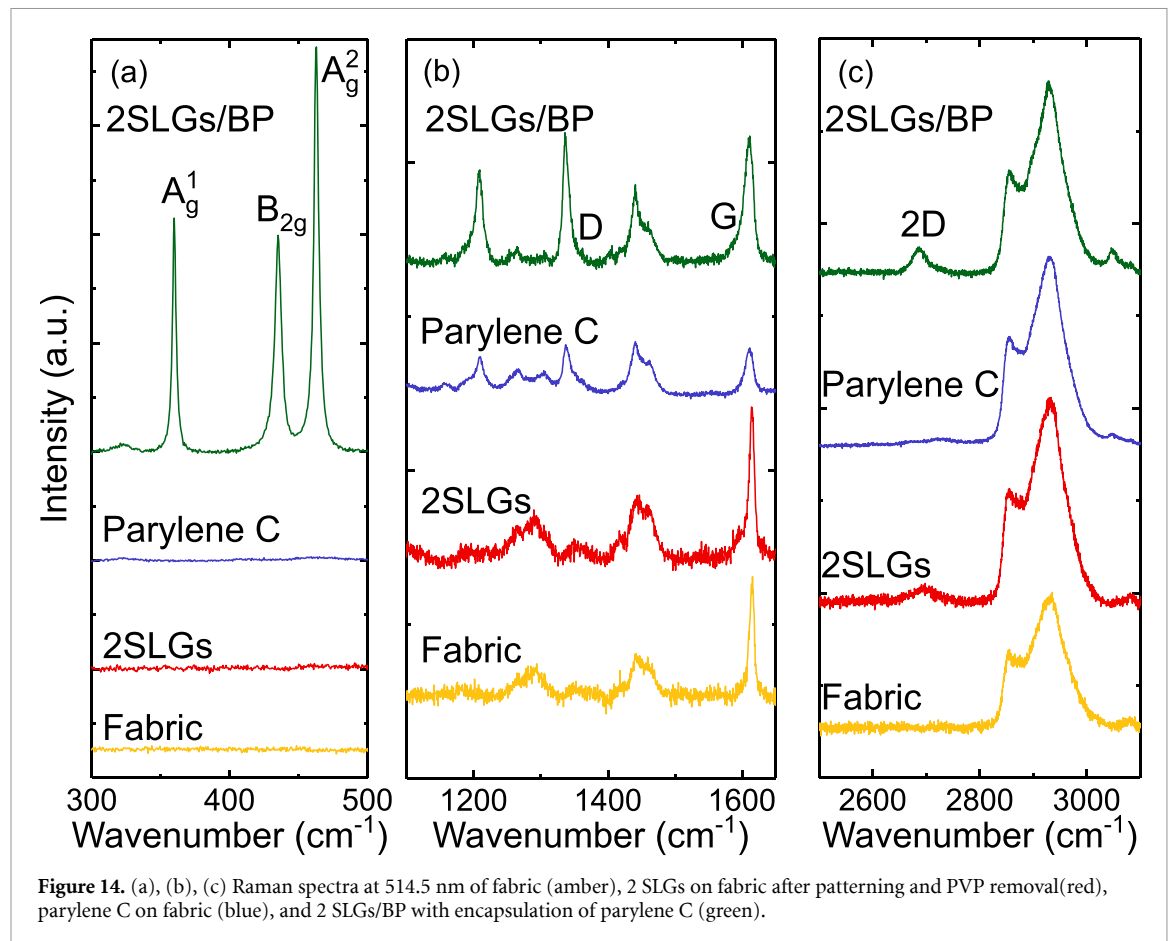$$D^* = \frac{(A_{\text{PD}}B)^{1/2}}{\text{NEP}} \tag{15}$$

where B is the electrical bandwidth(Hz), defined as difference between the upper and lower frequencies of R_{ext}, and NEP is the noise equivalent power (i.e. the power that gives a signal to noise ratio of one in a 1 Hz output bandwidth [6, 166]):

$$\text{NEP} = \frac{i_n}{R_{\text{ext}}}, \tag{16}$$

where i_n is the dark noise current, i.e. the current that exists when no light is incident on the PD [6]. The noise [A/$\sqrt{Hz}$] is measured in the time domain, by collecting the trace on an oscilloscope, with subsequent Fourier transform in order to analyze the data in the spectral domain. Figure 13(b) plots the 1/f noise (where f is the frequency). 1/f is the noise density (noise power per unit of bandwidth [dBm.Hz$^{-1/2}$] [6]), due to charge traps and defects [6]. At 4 Hz, ~ 5 times less than the cut off f, i.e. the f at which the detector R$_{ext}$ decreases by 3 dB [6], we get NEP $\sim 1.8 \times 10^{-10} WHz^{-1/2}$ and $D^* \sim 2 \times 10^7$ Jones. The noise current in the shot noise limit (due to generation-recombination of e-h pairs and resistive current paths in PDs [6]) is defined as $i_n = (2qI_{dark})^{1/2}$ [166], where the total dark current combines the contribution of the unamplified SLG current I$_{dark(SLG)}$, and the amplified injection current from BP, I$_{dark(BP)}$, due to the thermal excitation of charge carriers in dark. The latter is orders of magnitube smaller compared to I$_{dark(SLG)} \sim 200$mA. Therefore, following the methodology presented in reference [166], in our devices the shot noise limited noise current is $i_n = (2qI_{dark(SLG)})^{1/2}$. Thus, in the shot noise limit, we can write D^* as [6]:

$$D^* = \frac{R_{\text{ext}}(AB)^{1/2}}{[2qI_{\text{dark(SLG)}}]^{1/2}}. \tag{17}$$

Equation (17) gives $D^* \sim 10^{11}$ Jones, ~ 3 times higher than reference [45] for inkjet-printed graphene/MoS$_2$ PDs. It is also ~ 3-4 orders of magnitude higher than reference [47] for PDs based on inkjet-printed MoS$_2$. We note that gain was not included in the D^* calculations in references [46, 47], which may have led to a D^* overestimation. Thus, our inkjet-printed PDs are suitable for detecting weak light intensities which compete with the detector noise [6].

Figure 14. (a), (b), (c) Raman spectra at 514.5 nm of fabric (amber), 2 SLGs on fabric after patterning and PVP removal(red), parylene C on fabric (blue), and 2 SLGs/BP with encapsulation of parylene C (green).
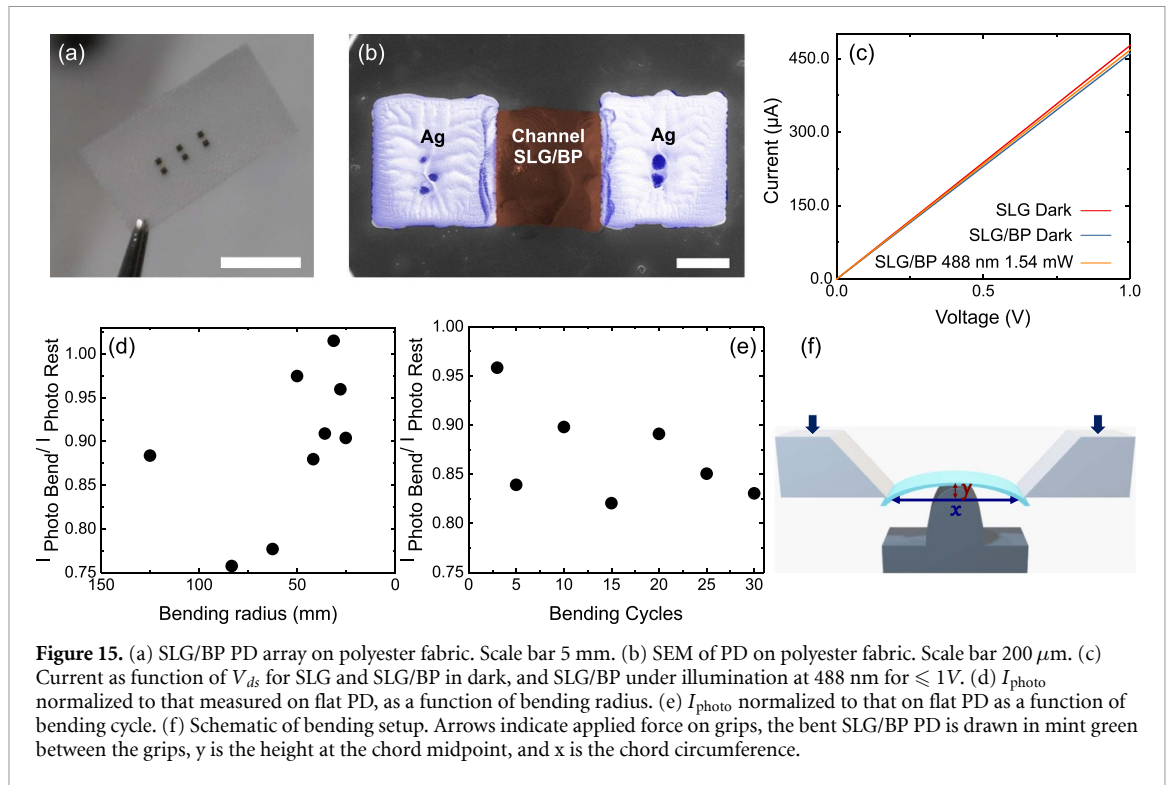
2.3. SLG/BP on fabric

In wearable applications, inkjet lithography has advantages over EBL and other lithography techniques for patterning and device fabrications because of textiles' porous [167], rough [167] and non-conductive structure [167], which makes these lithography techniques not suitable. To showcase this, we fabricate PDs on polyester fabric, because of its durability against Sun exposure [168], wrinkling [168] and shrinking [169], and common use ($\sim$52% of the synthetic textile market in 2018 [167, 170]). Since the surface roughness of textiles affects the electrical conductivity [171, 172], we planarize the surface by reducing the roughness. To do so, we rod coat polyurethane (PU) 10 times to reduce the root mean square (RMS) roughness from $\sim$50 μm to $< 5\mu m$. We then transfer SLG on PU coated polyester fabric using a similar procedure as for Si/SiO$_2$. After removing PMMA, a PVP ink is inkjet-printed as mask on SLG to pattern a $400\,\mu m \times 400\,\mu m$ channel. SLG is then etched via RIE, followed by removal of PVP with water.

Figure 14 shows the Raman spectra of 2 SLG on PU coated polyester fabric. The PU coated polyester fabric has two bands $\sim$2935 and $\sim$2845 cm^{-1} attributed to asymmetric and symmetric C-H stretching vibrations of CH$_2$ groups [173, 174], figure 14(c). The peak $\sim$1615 cm^{-1} can be ascribed to -C =

C- stretching vibrations of aromatic rings [175, 176], figure 14(b). The peak $\sim$1442 cm^{-1} can be assigned to C-H deformation vibrations of CH$_2$ groups [173, 176] and that $\sim$1251 cm^{-1} to coupled C-N and C-O vibrations of urethane [173, 176], figure 14(b). The spectrum of SLG on fabric has Pos(G)$\sim$1596.9 cm^{-1}, FWHM(G)$\sim$14.4 cm^{-1}, figure 14(b), Pos(2D)$\sim$2693.3 cm^{-1}, FWHM(2D) $\sim$56.6 cm^{-1}, figure 14(c). I(2D)/I(G) and A(2D)/A(G) are $\sim$1.5 and 5.8, indicating a p-doping of E$_F$$\sim$270 meV [132, 133], which corresponds to a carrier concentration $\sim$4.33$\times$10^{12} cm^{-2} [132]. I(D)/I(G)$\sim$1.03 corresponds to defect density $\sim$4.6$\times$10^{11}cm^{-2} [134, 135] for excitation energy 2.41 eV and E$_F$ = 270meV. For the E$_F$ derived from A(2D)/A(G), Pos(G) should be $\sim$1589.2 cm^{-1} for unstrained SLG [132]. In our experiments, Pos(G)$\sim$1596.9 cm^{-1}, which implies a contribution from uniaxial (biaxial) strain $\sim$0.33% (0.12%) [136], comparable to the uniaxial (biaxial) strain $\sim$0.36% (0.13%) of SLG on Si/SiO$_2$.

We then inkjet print electrodes with the Ag ink. The sample is annealed at $\sim$100 °C for $\sim$2 h to remove residual solvent (triethylene glycol monomethyl ether). We transfer two SLG to have $R_s$$\sim$2.1 K$\Omega$, comparable to transferred CVD SLG previously reported for polypropylene coated fabrics [172]. BP is then inkjet-printed on the channel layer.

Figure 15. (a) SLG/BP PD array on polyester fabric. Scale bar 5 mm. (b) SEM of PD on polyester fabric. Scale bar 200 μm. (c) Current as function of V_{ds} for SLG and SLG/BP in dark, and SLG/BP under illumination at 488 nm for $\leqslant 1V$. (d) I_{photo} normalized to that measured on flat PD, as a function of bending radius. (e) I_{photo} normalized to that on flat PD as a function of bending cycle. (f) Schematic of bending setup. Arrows indicate applied force on grips, the bent SLG/BP PD is drawn in mint green between the grips, y is the height at the chord midpoint, and x is the chord circumference.

Figures 15(a) and (b) are optical and SEM images of PDs on polyester fabric. Figure 15(c) plots the current–voltage characteristic in dark, which shows an Ohmic resistance ($R = 2.09\,K\Omega$) between inkjet-printed electrodes and SLG channel. We then characterize R_{ext} at 488 nm for P = 1.1 mW. Figure 15(c) shows that the current increases under illumination. We get $R_{ext}\sim6$ mA W^{-1} at 488 nm.

The Raman spectrum of BP coated on SLG on fabric is in figure 14(a). Pos(G)$\sim$1587.4 cm^{-1}, FWHM(G) broadens from $\sim$14.4 cm^{-1} to $\sim$15.6 cm^{-1}, figure 14(b), Pos(2D)$\sim$2687.5 cm^{-1}, FWHM(2D) narrows from $\sim$56.6 cm^{-1} to $\sim$32.5 cm^{-1}, figure 14(c). I(2D)/I(G) and A(2D)/A(G) are $\sim$5.1 and 10.7, indicating n-doping with $E_F\sim$100meV [132, 133] which corresponds to a carrier concentration $\sim0.7\times10^{12}$cm^{-2} [132]. I(D)/I(G) $\sim$5.2 gives a defect density $\sim1.4\times10^{12}$cm^{-2} [134, 135] for excitation energy 2.41 eV and $E_F\sim$100 meV. E_F estimated from A(2D)/A(G) would imply Pos(G)$\sim$1583.8 cm^{-1} for unstrained SLG [132]. However, in our experiments Pos(G)$\sim$1587.4 cm^{-1}, which would imply a contribution from uniaxial (biaxial) strain $\sim$0.15% (0.05%) [136].

Bendable devices, able to coordinate with body motions, such as arms' and legs' bending or extension, are appealing for wearable electronics. Thus, we test I_{photo} as function of bending using a Deben Microtest setup, figure 15(f). The bending radius R_b is defined as [177]:

$$R_b = \frac{y^2 + (x/2)^2}{2y},\qquad(18)$$

where y is the height at the chord midpoint and x is the chord circumference connecting the two ends of the grips, figure 15(f). To compare the performance at different R_b, the photocurrent at each R_b ($I_{Photo\ Bend}$) is normalized to that measured in flat conditions ($I_{Photo\ Rest}$). Figure 15(d) shows a change $\sim$17% of $\frac{I_{Photo\ Bend}}{I_{Photo\ Rest}}$ for R_b from flat to 25 mm. This is comparable to that reported for LMs-based PDs, such as InSe PDs on PET [178], but in reference [178] R_{ext} was $\sim$50% that of $R_b = 30$ mm [178]. Comparable R_b was reported for flexible ZnO nanowires [179], with on/off ratio $\sim11\times10^4$ ($I_d\sim$120nA) under $\sim$4.5 mWcm^{-2} of UV light (R_{ext} not reported) [179]. However the operating voltage (1 V) of our PDs is 3 times smaller than that in reference [179], making them more suitable for wearable applications, and lowering power. The SLG/BP PDs performance as a function of bending cycles, where 1 bending cycle is set at $R_b\sim$35 mm, is in figure 15(e). Our PDs retain $\sim$82% of $\frac{I_{Photo\ Bend}}{I_{Photo\ Rest}}$ for up to 30 cycles, comparable to what previously reported for CVD based MoS$_2$/SLG PDs on PET [180], making our approach promising for wearable and flexible applications.

3. Discussion

Our PDs on Si/SiO$_2$ have R_{ext} up to $\sim$337A W^{-1} at 488 nm for 1 V bias and work in the range $\sim$488 nm–2.7 μm. Reference [181] prepared PDs by depositing $\sim$30 nm thick WS$_2$ by rubbing WS$_2$ powder against a polycarbonate substrate. Then, Au(100 nm)/Ti(5 nm) electrodes were made using e-beam evaporation through a shadow mask. The

WS$_2$-based PDs showed R$_{ext}$~144 mA W^{-1} at 625 nm and V$_{ds}$~10 V, worse than ours, because of the photoconductive gain enhancement in our inkjet-printed hybrid SLG/BP PDs. Reference [182] presented WS$_2$-based PDs using ~4 nm WS$_2$ fabricated via RF magnetron sputtering, with R$_{ext}$~1.68 mA W^{-1} at 405 nm [182]. This is worse than ours because of the photoconductive gain mechanism in our hybrid SLG/BP PDs. Reference [183] measured R$_{ext}$~0.16 A W^{-1} at 405 nm in self-powered PDs based on oxidized WS$_2$(O-WS$_2$)/WS$_2$ heterojunctions, where ~7.2 nm WS$_2$ was transferred onto Si/SiO$_2$ by polydimethylsiloxane (PDMS)-assisted micromechanical exfoliation. Photoresist was then spin-coated on WS$_2$ via e-beam PHL, followed by oxygen plasma irradiation to form selective oxidation regions. Then, Au(100 nm)/Ti(10 nm) electrodes were prepared by PHL and electron beam deposition [183]. The fabrication process is more complex than ours, and the resulting R$_{ext}$ is ~2000 times lower, since no bias is applied through source and drain electrodes to dissociate photogenerated charges. Reference [184] used spin-coated carbon QDs on CVD 1 L-MoS$_2$ to achieve R$_{ext}$~377 A W^{-1} at 360 nm and 5 V. While R$_{ext}$ is comparable to ours, the PDs in reference [184] operated at 5 V and only between 300-700 nm, due to the spectral coverage of the carbon QDs [184], while our PDs work at 1 V from 488 nm to 2.7 μm. Reference [185] reported MoS$_2$-based PDs, prepared by abrasion of MoS$_2$ crystals (thickness ~15–25 μm) on the substrate, resulting in R$_{ext}$~1.5 μ A W^{-1} at 660 nm and V$_{ds}$~20 V. R$_{ext}$ and operation voltage are worse than ours, because of our photoconductive gain, combined with the use of BP as photoactive material. To the best of our knowledge, our SLG/BP PDs on Si/SiO$_2$ have the highest R$_{ext}$ amongst inkjet-printed LM-based PDs, and our operation wavelength range (488–2700 nm) is the broadest, as summarized in table 1.

For SLG/BP PDs on fabric we get R$_{ext}$~6 mA W^{-1} at 488 nm, i.e. ~56 000 less than on SLG/BP PDs on Si/SiO$_2$. This R$_{ext}$ decrease is expected, since the photogenerated h in the BP VB experience weaker electric fields at the SLG/BP interface (p-doping ~270 meV) compared to the SLG/BP interface (n-doping ~360 meV) on Si/SiO$_2$. Moreover, μ for SLG on fabric is lower than that on Si/SiO$_2$, and the channel in our PDs on fabric is ~8 times larger than on Si/SiO$_2$. R$_{ext}$ also decreases when the optical power increases, due to the increase in scattering of photogenerated carriers in the channel [165], and Auger recombination induced by increasing power [165].

To the best of our knowledge, there is no report of inkjet-printed textile PDs based on LMs. Our R$_{ext}$ is ~6 times higher than inkjet-printed SLG/WS$_2$ PDs on PET [42], and one order of magnitude higher (R$_{ext}$~0.11 mA W^{-1} at 405 nm [100]) than CVD SLG based PDs on flexible (acrylic) substrates [100].

4. Conclusions

We reported an inkjet printing-based approach to prepare PDs, combining CVD SLG and binder-free LPE BP. The devices have R$_{ext}$ up to ~337 A W^{-1} at 488 nm, and ~48 mA W^{-1} at 2700 nm, with operation voltage $\leqslant 1V$. We used this to make flexible PDs on polyester fabric. These PDs were investigated as function of bending radius and cycles. The responsivity, flexibility, and low operation voltage of our PDs makes them attractive for wearable and low-power optoelectronic applications.

Data availability statement

All data that support the findings of this study are included within the article (and any supplementary files). DOI: https://doi.org/10.17863/CAM.91144

ORCID iDs

S Akhavan ● https://orcid.org/0000-0003-1525-4196
S Doukas ● https://orcid.org/0000-0003-3903-4569
K Dimos ● https://orcid.org/0000-0001-7390-1289
L G Occhipinti ● https://orcid.org/0000-0002-9067-2534
A C Ferrari ● https://orcid.org/0000-0003-0907-9993

References

[1] Fowler B, Liu C, Mims S, Balicki J, Li W, Do H, Appelbaum J and Vu P 2010 *Proc. SPIE* **7536** 753607
[2] Mueller T, Xia F and Avouris P 2010 *Nat. Photon.* **4** 297
[3] Kallhammer J-E 2006 *Nat. Photon.* **5** 12
[4] Formisano V, Atreya S, Encrenaz T, Ignatiev N and Giuranna M 2004 *Science* **306** 1758
[5] Koppens F H L, Mueller T, Avouris P, Ferrari A C, Vitiello M S and Polini M 2014 *Nat. Nanotechnol.* **9** 780
[6] Sze S M and Ng K K 2006 *Physics of Semiconductor Devices* (New York: Wiley)
[7] Henini M and Razeghi M 2002 *Handbook of Infrared Detection Technologies* (Amsterdam: Elsevier)
[8] Miller D A B 2000 *Proc. IEEE* **88** 728
[9] Jiang J, Mi K, Tsao S, Zhang W, Lim H, O'Sullivan T, Sills T, Razeghi M, Brown G J and Tidrow M Z 2004 *Appl. Phys. Lett.* **84** 2232
[10] Leia W, Antoszewski J and Faraone L 2015 *Appl. Phys. Lett.* **2** 041303
[11] Ferrari A C *et al* 2015 *Nanoscale* **7** 4598
[12] Konstantatos G, Badioli M, Gaudreau L, Osmond J, Bernechea M, De Arquer F P G, Gatti F and Koppens F H L 2012 *Nat. Nanotechnol.* **7** 363

[13] Nikitskiy I, Goossens S, Kufer D, Lasanta T, Navickaite G, Koppens F H L and Konstantatos G 2016 *Nat. Commun.* **7** 1

[14] Ma P, Salamin Y, Baeuerle B, Josten A, Heni W, Emboras A and Leuthold J 2018 *ACS Photonics* **6** 154

[15] Liu C H, Chang Y C, Norris T B and Zhong Z 2014 *Nat. Nanotechnol.* **9** 273

[16] Viti L, Purdie D G, Lombardo A, Ferrari A C and Vitiello M S 2020 *Nano Lett.* **20** 3169–77

[17] Asgari M *et al* 2021 *ACS Nano* **15** 17966–76

[18] Goossens S *et al* 2017 *Nat. Photon.* **11** 366

[19] Tan H, Fan Y, Zhou Y, Chen Q, Xu W and Warner J H 2016 *ACS Nano* **10** 7866

[20] Chen T, Sheng Y, Zhou Y, Chang R-J, Wang X, Huang H, Zhang Q, Hou L and Warner J H 2019 *ACS Appl. Mater. Interfaces* **11** 6421

[21] Kufer D, Nikitskiy I, Lasanta T, Navickaite G, Koppens F H L and Konstantatos G 2015 *Adv. Mater.* **27** 176

[22] Konstantatos G 2018 *Nat. Commun.* **9** 1

[23] Özdemir O, Ramiro I, Gupta S and Konstantatos G 2019 *ACS Photonics* **6** 2381

[24] Huo N, Gupta S and Konstantatos G 2017 *Adv. Mater.* **29** 1606576

[25] Lee E J H, Balasubramanian K, Weitz R T, Burghard M and Kern K 2008 *Nat. Nanotechnol.* **3** 486

[26] Bonaccorso F, Sun Z, Hasan T and Ferrari A C 2010 *Nat. Photon.* **4** 611

[27] Kobayashia T *et al* 2013 *Appl. Phys. Lett.* **102** 023112

[28] Brida D *et al* 2013 *Nat. Commun.* **4** 1

[29] Lee Y, Kwon J, Hwang E, Ra C-H, Yoo W J, Ahn J-H, Park J H and Cho J H 2015 *Adv. Mater.* **27** 41–46

[30] Backes C *et al* 2020 *2D Mater.* **7** 022001

[31] Hernandez Y *et al* 2008 *Nat. Nanotechnol.* **3** 563

[32] Torrisi F *et al* 2012 *ACS Nano* **6** 2992

[33] Karagiannidis P G *et al* 2017 *ACS Nano* **11** 2742

[34] Bonaccorso F, Lombardo A, Hasan T, Sun Z, Colombo L and Ferrari A C 2012 *Mater. Today* **15** 564

[35] Kaur H and Coleman J N 2022 *Adv. Mater.* **15** 2202164

[36] Dodoo-Arhin D, Howe R C T, Hu G, Zhang Y, Hiralal P, Bello A, Amaratunga G and Hasan T 2016 *Carbon* **105** 33

[37] Yang J, Voiry D, Ahn S J, Kang D, Kim A Y, Chhowalla M and Shin H S 2013 *Angew. Chem., Int. Ed. Engl.* **52** 13751

[38] Bonaccorso F, Colombo L, Yu G, Stoller M, Tozzini V, Ferrari A C, Ruoff R S and Pellegrini V 2015 *Science* **347** 1246501

[39] Li J, Ye F, Vaziri S, Muhammed M, Lemme M C and Östling M 2013 *Adv. Mater.* **25** 3985

[40] Finn D J, Lotya M, Cunningham G, Smith R J, McCloskey D, Donegan J F and Coleman J N 2014 *J. Mater. Chem. C* **2** 925

[41] Hu G *et al* 2017 *Nat. Commun.* **8** 278

[42] McManus D *et al* 2017 *Nat. Nanotechnol.* **12** 343

[43] Lee K, Kim H-Y, Lotya M, Coleman J N, Kim G-T and Duesberg G S 2011 *Adv. Mater.* **23** 4178

[44] Lee Y, Yang J, Lee D, Kim Y-H, Park J-H, Kim H and Ho Cho J 2016 *Nanoscale* **8** 9193

[45] Hossain R F, Deaguero I G, Boland T and Kaul A B 2017 *npj 2D Mater. Appl.* **1** 1

[46] Li J, Naiini M M, Vaziri S, Lemme M C and Östling M 2014 *Adv. Funct. Mater.* **24** 6524

[47] Seo J-W T, Zhu J, Sangwan V K, Secor E B, Wallace S G and Hersam M C 2019 *Appl. Mater. Interfaces* **11** 5675

[48] Morita A 1986 *Appl. Phys. A* **39** 227

[49] Xia F, Wang H, Xiao D, Dubey M and Ramasubramaniam A 2014 *Nat. Photon.* **8** 899

[50] Chang T-Y, Chen P-L, Yan J-H, Li W-Q, Zhang Y-Y, Luo D-I, Li J-X, Huang K-P and Liu C-H 2019 *ACS Appl. Mater. Interfaces* **12** 1201

[51] Chen X *et al* 2017 *Nat. Commun.* **8** 1672

[52] Buscema M, Groenendijk D J, Blanter S I, Steele G A, van der Zant H S J and Castellanos-Gomez A 2014 *Nano Lett.* **14** 3347

[53] Huang M, Wang M, Chen C, Ma Z, Li X, Han J and Wu Y 2016 *Adv. Mater.* **28** 3481

[54] Huang L *et al* 2018 *ACS Nano* **13** 913

[55] Bullock J *et al* 2018 *Nat. Photon.* **12** 601

[56] Guo Q *et al* 2016 *Nano Lett.* **16** 4648

[57] Engel M, Steiner M and Avouris P 2014 *Nano Lett.* **14** 6414

[58] Huang Y *et al* 2020 *Nat. Commun.* **11** 1

[59] Novoselov K S, Geim A K, Morozov S, Jiang D, Katsnelson M, Grigorieva I, Dubonos S and Firsov A A 2005 *Nature* **438** 197

[60] Castellanos-Gomez A *et al* 2014 *2D Mater.* **1** 025001

[61] Kou L, Chen C and Smith S C 2015 *J. Phys. Chem. Lett.* **6** 2794

[62] Smith J B, Hagaman D and Ji H-F 2016 *Nanotechnology* **27** 215602

[63] Hanlon D *et al* 2015 *Nat. Commun.* **6** 8563

[64] Kang J, Wood J D, Wells S A, Lee J-H, Liu X, Chen K-S and Hersam M C 2015 *ACS Nano* **9** 3596

[65] Kang J, Wells S A, Wood J D, Lee J-H, Liu X, Ryder C R, Zhu J, Guest J R, Husko C A and Hersam M C 2016 *Proc. Natl Acad. Sci.* **113** 11688

[66] Zhou G, Li Z, Ge Y, Zhang H and Sun Z 2020 *Nanoscale Adv.* **2** 1059

[67] Yuan H *et al* 2015 *Nat. Nanotechnol.* **10** 707

[68] Liu Y *et al* 2017 *ACS Appl. Mater. Interfaces* **9** 36137

[69] Kim T-Y, Ha J, Cho K, Pak J, Seo J, Park J, Kim J-K, Chung S, Hong Y and Lee T 2017 *ACS Nano* **11** 10273

[70] Withers F *et al* 2014 *Nano Lett.* **14** 3987

[71] Miao J, Song B, Li Q, Cai L, Zhang S, Hu W, Dong L and Wang C 2017 *ACS Nano* **11** 6048

[72] Saleh B E and Teich M C 2019 *Fundamentals of Photonics* (Hoboken, NJ: Wiley)

[73] Pan K, Fan Y, Leng T, Li J, Xin Z, Zhang J, Hao L, Gallop J, Novoselov K S and Hu Z 2008 *Nat. Commun.* **9** 5179

[74] Carey B, *et al* 2017 *Nat. Commun.* **8** 14482

[75] Bariyam M *et al* 2018 *ACS Nano* **12** 6978

[76] Nathan A *et al* 2012 *Proc. IEEE* **100** 1486

[77] Yang L, Rida A, Vyas R and Tentzeris M M 2007 *IEEE Trans. Microw. Theory Tech.* **55** 2894

[78] Jaakkola K, Ermolov V, Karagiannidis P G, Hodge S A, Lombardi L, Zhang X, Grenman R, Sandberg H, Lombardo A and Ferrari A C 2019 *2D Mater.* **7** 015019

[79] Tudorache M and Bala C 2007 *Anal Bioanal. Chem.* **388** 565

[80] Bharathan J and Yang Y 1998 *Appl. Phys. Lett.* **72** 2660

[81] Hammock M L, Chortos A, Tee B C-K, Tok J B-H and Bao Z 2013 *Adv. Mater.* **25** 5997

[82] Shaheen S E, Radspinner R, Peyghambarian N and Jabbour G E 2001 *Appl. Phys. Lett.* **79** 2996

[83] Cao X, Chen H, Gu X, Liu B, Wang W, Cao Y, Wu F and Zhou C 2014 *ACS Nano* **8** 12769

[84] Lau P H, Takei K, Wang C, Ju Y, Kim J, Yu Z, Takahashi T, Cho G and Javey A 2013 *Nano Lett.* **13** 3864

[85] Higuchi K, Kishimoto S, Nakajima Y, Tomura T, Takesue M, Hata K, Kauppinen E I and Ohno Y 2013 *Appl. Phys. Express* **6** 085101

[86] Secor E B, Prabhumirashi P L, Puntambekar K, Geier M L and Hersam M C 2013 *J. Phys. Chem. Lett.* **4** 1347

[87] Ng L W, Hu G, Howe R C, Zhu X, Yang Z, Jones C and Hasan T 2019 *Printing of Graphene and Related 2D Materials* (Berlin: Springer)

[88] Kelly A G *et al* 2017 *Science* **356** 69

[89] Sirringhaus H, Kawase T, Friend R H, Shimoda T, Inbasekaran M, Wu W and Woo E P 2000 *Science* **290** 2123

[90] Sekitani T, Noguchi Y, Zschieschang U, Klauk H and Someya T 2008 *Proc. Natl Acad. Sci. USA* **105** 4976

[91] Hu G, Ng L W T, Zhu X, Howe R C T and Hasan T 2018 *Chem. Soc. Rev.* **47** 3265

[92] Hutchings I M and Graham D 2012 *Inkjet Technology for Digital Fabrication* (Hoboken, NJ: Wiley)

[93] Noh Y-Y, Zhao N, Caironi M and Sirringhaus H 2007 *Nat. Nanotechnol.* **2** 784

[94] Kawase T, Sirringhaus H, Friend R H and Shimoda T 2001 *Adv. Mater.* **13** 1601

[95] Hondred J A, Stromberg L R, Mosher C L and Claussen J C 2017 *ACS Nano* **11** 9836

[96] Favron A, Gaufrés E, Fossard F, Phaneuf-L'Heureux A-L, Tang N Y-W, Lévesque P L, Loiseau A, Leonelli R, Francoeur S and Martel R 2015 *Nat. Mater.* **14** 826

[97] Kam K K and Parkinson B A 1982 *J. Phys. Chem.* **86** 463–7

[98] Splendiani A, Sun L, Zhang Y, Li T, Kim J, Chim C-Y, Galli G and Wang F 2010 *Nano Lett.* **10** 1271–5

[99] Wang S, Ang P K, Wang Z, Tang A L L, Thong J T L and Loh K P 2010 *Nano Lett.* **10** 92–98

[100] Kang P, Wang M C, Knapp P M and Nam S 2016 *Adv. Mater.* **28** 4639

[101] Bonaccorso F, Hasan T, Tan P H, Sciascia C, Privitera G, Di Marco G, Gucciardi P G and Ferrari A C 2010 *J. Phys. Chem. C* **114** 17267

[102] Liu H, Neal A T, Zhu Z, Luo Z, Xu X, Tománek D and Ye P D 2014 *ACS Nano* **8** 4033

[103] Xia F, Wang H and Jia Y 2014 *Nat. Commun.* **5** 1

[104] Akahama Y, Kobayashi M and Kawamura H 1997 *Solid State Commun.* **104** 311

[105] Wang X, Mao N, Luo W, Kitadai H and Ling X 2018 *J. Phys. Chem. Lett.* **9** 2830

[106] Ribeiro H B, Pimentab M A and de Matos C J S 2018 *J. Raman Spectrosc.* **49** 76

[107] Ribeiro H B, Villegas C E P, Bahamon D A, Muraca D, Castro Neto A H, de Souza E A T, Rocha A R, Pimenta M A and de Matos C J S 2016 *Nat. Commun.* **7** 1

[108] Derby B and Reis N 2003 *MRS Bull.* **28** 815

[109] Derby B 2010 *Annu. Rev. Mater. Res.* **40** 395

[110] Fromm J E 1984 *IBM J. Res. Dev.* **28** 322

[111] Deegan R D, Bakajin O, Dupont T F, Huber G, Nagel S R and Witten T A 1997 *Nature* **389** 827

[112] Secor E B, Ahn B Y, Gao T Z, Lewis J A and Hersam M C 2015 *Adv. Mater.* **27** 6683

[113] Lotya M *et al* 2009 *J. Am. Chem. Soc.* **131** 3611

[114] Lide D R *et al* 2005 *CRC Handbook of Chemistry and Physics* vol 89 (Boca Raton, FL: CRC Press) p 3

[115] Lee K P, Chromey N C, Culik R, Barnes J R and Schneider P W 1987 *Fundam. Appl. Toxicol.* **9** 222

[116] (Available at: https://apps.who.int/iris/handle/10665/42404)

[117] Lin S *et al* 2016 *Adv. Funct.* **26** 864

[118] Wood J D, Wells S A, Jariwala D, Chen K-S, Cho E, Sangwan V K, Liu X, Lauhon L J, Marks T J and Hersam M C 2014 *Nano Lett.* **14** 6964

[119] Goodman N B, Ley L and Bullett D 1983 *Phys. Rev. B* **27** 7440

[120] Brunner J, Thüler M, Veprek S and Wild R 1979 *J. Phys. Chem. Solids* **40** 967

[121] Ashurst J V and Nappe T M 2019 *Methanol Toxicity* (Treasure Island, FL: StatPearls Publishing)

[122] Li L, Yu Y, Ye G J, Ge Q, Ou X, Wu H, Feng D, Chen X H and Zhang Y 2014 *Nat. Nanotechnol.* **9** 372

[123] Bunsen R and Roscoe H E 1857 *Ann. Phys.* **162** 235–63

[124] Beer B 1852 *Ann. Physik* **162** 78–88

[125] Luther R and Nikolopulos A 1913 *Z. Phys. Chem.* **82 U** 361

[126] Swinehart D F 1962 *J. Chem. Educ.* **39** 333

[127] Harada Y, Murano K, Shirotani I, Takahashi T and Maruyama Y 1982 *Solid State Commun.* **44** 877

[128] Bae S *et al* 2010 *Nat. Nanotechnol.* **5** 574

[129] Lagatsky A A *et al* 2013 *Appl. Phys. Lett.* **1** 013113

[130] Ferrari A C *et al* 2006 *Phys. Rev. Lett.* **97** 187401

[131] Ferrari A C and Basko D M 2013 *Nat. Nanotechnol.* **8** 235

[132] Das A *et al* 2008 *Nat. Nanotechnol.* **3** 210

[133] Basko D M, Piscanec S and Ferrari A C 2009 *Phys. Rev. B* **80** 165413

[134] Cançado L G, Jorio A, Ferreira E H M, Stavale F, Achete C, Capaz R, Moutinho M, Lombardo A, Kulmala T and Ferrari A C 2011 *Nano Lett.* **11** 3190

[135] Bruna M, Ott A K, Ijäs M, Yoon D, Sassi U and Ferrari A C 2014 *ACS Nano* **8** 7432

[136] Mohiuddin T M G *et al* 2009 *Phys. Rev. B* **79** 205433

[137] Yoon D, Son Y-W and Cheong H 2011 *Phys. Rev. Lett.* **106** 155502

[138] Pisana S, Lazzeri M, Casiraghi C, Novoselov K S, Geim A K, Ferrari A C and Mauri F 2007 *Nat. Mater.* **6** 198

[139] Casiraghi C, Pisana S, Novoselov K S, Geim A K and Ferrari A C 2007 *Appl. Phys. Lett.* **91** 233108

[140] Du C, Wang S, Miao X, Sun W, Zhu Y, Wang C and Ma R 2019 *Beilstein J. Nanotechnol.* **10** 2374

[141] Jirgensons B 1952 *J. Polym. Sci.* **8** 519

[142] Geim A K and Novoselov K S 2007 *Nat. Mater.* **6** 183

[143] Xia J, Chen F, Li J and Tao N 2009 *Nat. Nanotechnol.* **4** 505

[144] Zhang Y, Tan Y-W, Stormer H L and Kim P 2005 *Nature* **438** 201

[145] Adam S, Hwang E, Galitski V and Sarma S D 2007 *Proc. Natl Acad. Sci. USA* **104** 18392

[146] Chen J-H, Jang C, Adam S, Fuhrer M, Williams E and Ishigami M 2008 *Nat. Phys.* **4** 377

[147] Galitski V M, Adam S and Sarma S D 2007 *Phys. Rev. B* **76** 245405

[148] Chua L-L, Zaumseil J, Chang J-F, Ou E C-W, Ho P K-H, Sirringhaus H and Friend R H 2005 *Nature* **434** 194–9

[149] Fukuda K, Yokota T, Kuribara K, Sekitani T, Zschieschang U, Klauk H and Someya T 2010 *Appl. Phys. Lett.* **96** 17

[150] Mathur M S and Weir N A 1973 *J. Mol. Struct.* **15** 459

[151] Jakabovic J, Kovacac J, Weisb M, Haskoc D, Srnaneka R, Valenta P and Reseld R 2009 *Microelectronics J.* **40** 595

[152] Yamada T, Okigawa Y, Hasegawa M, Watanabe K and Taniguchi T 2020 *AIP Adv.* **10** 085309

[153] Meric I, Han M Y, Young A F, Ozyilmaz B, Kim P and Shepard K L 2008 *Nat. Nanotechnol.* **3** 654

[154] Lazzeri M, Piscanec S, Mauri F, Ferrari A C and Robertson J 2005 *Phys. Rev. Lett.* **95** 236802

[155] Xia F, Mueller T, Golizadeh-Mojarad R, Freitag M, Lin Y-M, Tsang J, Perebeinos V and Avouris P 2009 *Nano Lett.* **9** 1039–44

[156] Xia F, Mueller T, Lin Y-M, Valdes-Garcia A and Avouris P 2009 *Nat. Nanotechnol.* **4** 839–43

[157] Yasaei P, Kumar B, Foroozan T, Wang C, Asadi M, Tuschel D, Indacochea J E, Klie R F and Salehi-Khojin A 2015 *Adv. Mater.* **27** 1887

[158] Ingle J D Jr and Crouch S R 1988 *Spectrochemical Analysis* (Upper Saddle River, NJ,: Prentice Hall)

[159] Liu H, Du Y, Deng Y and Ye P D 2015 *Chem. Soc. Rev.* **44** 2732

[160] Lucarini V, Saarinen J J, Peiponen K E and Vartiainen E M 2005 *Kramers-Kronig Relations in Optical Materials Research* (Berlin: Springer)

[161] (Available at: https://airekacells.com/blog/cuvette-guide)

[162] Lampadariou E, Kaklamanis K, Goustouridis D, Raptis I and Lidorikis E 2022 *Photonics* **9** 499

[163] Hanson G W 2008 *J. Appl. Phys.* **44** 084314

[164] Velusamy D B *et al* 2015 *Nat. Commun.* **6** 1

[165] Mudd G W *et al* 2015 *Adv. Mater.* **27** 3760

[166] Bianconi S, Lauhon L and Mohseni H 2021 *Nat. Photon.* **15** 714

[167] McCann J and Bryson D 2009 *Smart Clothes and Wearable Technology* (Amsterdam: Elsevier)

[168] Hearle J W S and Morton W E 2008 *Physical Properties of Textile Fibres* (Amsterdam: Elsevier)

[169] Annis P A 2012 *Understanding and Improving the Durability of Textiles* (Amsterdam: Elsevier)

[170] Pepper L R and Materson E Preferred Fiber and Materials Market Report 2017 2019 (Textile Exchange)

[171] Kim N *et al* 2020 *Nat. Commun.* **11** 1424

[172] Neves A I S, Bointon T H, Melo L V, Russo S, de Schrijver I, Craciun M F and Alves H 2015 *Sci. Rep.* **5** 9866

[173] Socrates G 2001 *Infrared and Raman Characteristic Group Frequencies* 3rd edn (Hoboken, NJ: Wiley)

[174] Bruckmoser K and Resch K 2014 *Macromol. Symp* **339** 70

[175] Parnell S, Min K and Cakmak M 2003 *Polymer* **44** 5137

[176] Ezhil Vilian A T, An S, Choe S R, Kwak C H, Huh Y S, Lee J and Han Y-K 2016 *Biosens. Bioelectron.* **86** 122

[177] Hearle J W S, Grosberg P and Backer S 1969 *Structural Mechanics of Fibers, Yarns and Fabrics* (Hoboken, NJ: Wiley)

[178] Reddy Tamalampudi S, Lu Y-Y, Kumar R, Sankar R, Liao C-D, Moorthy K, Cheng C-H, Chou F and Chen Y-T 2014 *Nano Lett.* **14** 2800

[179] Bai S, Wu W, Qin Y, Cui N, Bayerl D J and Wang X 2011 *Adv. Funct. Mater.* **23** 4464

[180] De Fazio D *et al* 2016 *ACS Nano* **10** 8252

[181] Quereda J, Kuriakose S, Munuera C, Mompean F J, Enizi A M A, Nafady A, Diez E, Frisenda R and Castellanos-Gomez A 2022 *npj Flex. Electron.* **6** 1–9

[182] Kim B H, Gu H H and Yoon Y J 2018 *2D Mater.* **5** 045030

[183] Lu J, Ye Q, Ma C, Zheng Z, Yao J and Yang G 2022 *ACS Nano* **8** 12852–65

[184] Liu H, Gao F, Hu Y, Zhang J, Wang L, Feng W, Hou J and Hu P 2019 *2D Mater.* **6** 035025

[185] Mazaheri A, Lee M, van der Zant H S J, Frisenda R and Castellanos-Gomez A 2020 *Nanoscale* **12** 19068–74